Nanoimaging and Nanospectroscopy of Polaritons with Time Resolved *s*-SNOM

Ziheng Yao[1,†], Suheng Xu[1,†], Debo Hu[2,†], Xinzhong Chen[1], Qing Dai[2,], Mengkun Liu[1,*]*

Z. H. Yao, S. H. Xu, X. Z. Chen, Prof. M. K. Liu
Department of Physics and Astronomy, Stony Brook University, Stony Brook, NY 11794, USA
E-mail: mengkun.liu@stonybrook.edu

Dr. D. B. Hu, Prof. Q. Dai
Division of Nanophotonics, CAS Center for Excellence in Nanoscience, National Center for Nanoscience and Technology, Beijing 100190, China
E-mail: daiq@nanoctr.cn

Keywords: polaritonics, plasmon polaritons, phonon polaritons, *s*-SNOM

Abstract: The development of electronics and photonics is entering a new era of ultra-high-speed sensing, data processing, and telecommunication. The carrier frequencies of the next-generation electronic devices inevitably extend beyond radio frequencies, marching toward the nominally photonics-dominated territories, e.g. terahertz and beyond. As a result, electronic and photonic techniques naturally merge and seek common ground. At the forefront of this technical trend is the field of polaritonics, where polaritons are half-light, half-matter quasiparticles that carry the properties of both ‘bare’ photons and ‘bare’ dipole-carrying excitations. The Janus-faced nature of polaritons renders the unique capability of operando control using photoexcitation or applied electric field. This report reviews and comments on the state-of-the art ultrafast polaritonic phenomena probed by scattering-type scanning near-field optical microscope (*s*-SNOM) techniques. The ultrafast dynamical control and loss-reduction of the polariton propagation are discussed with special emphasis on the creation and probing of the tip or edge induced plasmon- and phonon-polaritons in low-dimensional systems. The detailed technical aspects of *s*-SNOM and its possible future development are also presented.

1. Introduction

Surface polaritons, a hybrid of electromagnetic wave and collective oscillation modes in materials,[1-4] have gained considerable attention for their potential applications in nanophotonic and quantum technologies. As a general solution of Maxwell's equations with well-defined boundary conditions,[5] surface polaritons have been widely accepted as a potent candidate for light manipulation due to their abundant material bases. The strong light-matter interactions provide chances to manipulate light with both electronic and photonic means.[6,7] The excellent optical responses of polaritons in THz and IR frequency ranges also enable many applications in bio-sensing and chemical identification.[8-10] One particular focus in this field is to search for better polaritonic systems with low optical loss, high coupling rate, and ultrafast tunability.[11]

In this review, we first briefly introduce the formation of surface polaritons. How the negative permittivity, which is a prerequisite for the existence of surface polaritons, origins from plasma, phonon or exciton resonances is briefly discussed. We then discuss how the near-field setup, especially the scattering-type scanning near-field microscopy (*s*-SNOM), will be useful for the excitation and characterization of the polaritons. The bulk part of this review is an overview of state-of-the-art ultrafast near-field experiments on polaritons in 2D materials. We focus on multi-facets including the experimental setup, main results, underlying mechanisms and the improvements that may be or have already been made. Finally, a brief outlook for the time resolved near-field detection of polaritons using *s*-SNOM will be presented.

2. Origins and Classification of Surface Polaritons

2.1. Optical Systems Supporting Surface Polaritons

To understand why materials can support surface polaritons in specific frequency ranges, we have to review the electromagnetic theory of polaritons and optical polarization of materials. In this section, we mathematically derive the polariton modes from Maxwell equations. All materials involved are assumed to be non-magnetic and therefore the relative permeabilities are equal to unity.[12] For systems with specific permittivity compositions, transverse magnetic (TM) polarized electromagnetic modes may exist. These modes are confined in one dimension and can propagate freely in the remaining two dimensions.

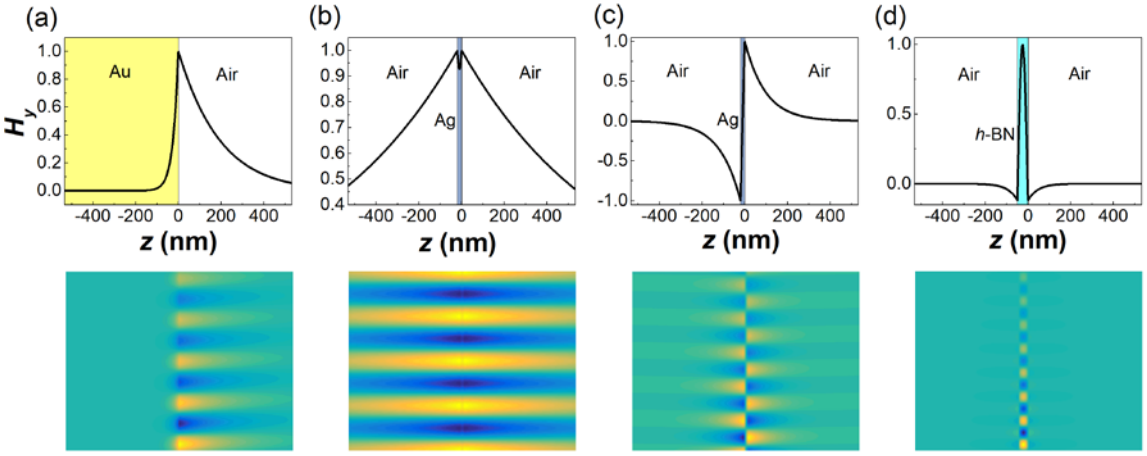

Figure 1 Field distributions of surface polaritons in different optical systems in the *z* direction (out-of-plane direction). The upper panels show the distributions of the magnetic component H_y. (a) Surface plasmon polaritons at the Au-Air interface. (b) and (c) Symmetric and anti-symmetric surface plasmon polaritons supported by ultrathin Ag film. (d) Surface phonon polaritons in *h*-BN thin slab. The lower panels display the simulated real space propagation process of each polaritonic mode in the upper panels. The color shows the strength of H_y. The lateral length scale is the same as in the upper panels. The upper panels can be regarded as a line cut in the corresponding lower panels.

2.1.1. Interface Between Two Media with Permittivities of Opposite Signs

Consider an interface between two materials. The interface lies in the plane labeled by z=0. The relative permittivities of this two materials are ε_1 and ε_2 respectively (see Figure 1a for schematics). The wave vectors or field components in each area will also be labeled by 1 or 2 correspondingly.

For surface polaritons, the field is confined at the interface. The proper way of showing the evanescent nature of the field is to make the solution for Maxwell's equations to take the following form:

$$\begin{cases} \mathbf{E}_1 e^{-\alpha_1 z} e^{i(qx-\omega t)} = (E_{1x}, E_{1y}, E_{1z}) e^{-\alpha_1 z} e^{i(qx-\omega t)} \\ \mathbf{E}_2 e^{\alpha_2 z} e^{i(qx-\omega t)} = (E_{2x}, E_{2y}, E_{2z}) e^{\alpha_2 z} e^{i(qx-\omega t)} \end{cases}, \tag{1}$$

where $\mathbf{E}_1$ and $\mathbf{E}_2$ are the electric fields, α_1 and α_2 are the decaying factors, and q is the in-plane wavevector. Apply the Gauss's law and the Faraday's law to **Equation 1.** After imposing the interface conditions that the in-plane field components (E_y and H_x for transverse electric (TE) polarized mode, H_y and E_x for TM polarized mode) are continuous, we get:

$$\begin{cases} E_{1y} = E_{2y} \\ \alpha_1 E_{1y} = -\alpha_2 E_{2y} \\ E_{1x} = E_{2x} \\ \dfrac{\varepsilon_1}{\alpha_1} E_{1x} = -\dfrac{\varepsilon_2}{\alpha_2} E_{2x} \end{cases}, \tag{2}$$

which means E_{1y}=E_{2y}=0 (no transverse electric field, TM mode only) and

$$\frac{\alpha_1}{\alpha_2} = -\frac{\varepsilon_1}{\varepsilon_2}. \tag{3}$$

Combining **Equation 3** with the fact that

$$\begin{cases} \alpha_1 = \sqrt{q^2 - k_0^2 \varepsilon_1} \\ \alpha_2 = \sqrt{q^2 - k_0^2 \varepsilon_2} \end{cases}, \; k_0 = \frac{\omega}{c} \tag{4}$$

we find:

$$q = k_0 \sqrt{\frac{\varepsilon_1 \varepsilon_2}{\varepsilon_1 + \varepsilon_2}} \tag{5}$$

Since the field strength decay exponentially with the distance away from the z=0 interface, α_1 and α_2 are both positive. According to Equation 3, the real part of ε_1 and ε_2 must possess opposite signs. Here ε_1 stands for the permittivity of the topmost layer, which, in the near-field experiment, is usually air or dielectric cover of the dispersive material. So usually ε_1 is positive and has a flat frequency response. On the other hand, $\varepsilon_2 = \varepsilon_2(\omega)$ is dispersive and can be negative. Noble metals such as gold and silver can exhibit negative permittivities in the visible frequency range and support surface polaritons at their interfaces with dielectrics. **Figure 1**a shows the calculated field distribution of H_y and the real space propagation of polaritons confined at the Au-Air interface at the wavelength of 532 nm. It can be observed that this polaritonic mode is tightly confined in the direction normal to the interface and can propagate freely along the interface, with certain damping.

2.1.2. Thin Film with Negative Permittivity

If the thickness d of the dispersive material is finite, polaritonic modes can be supported on both interfaces. Since α denotes the inverse of decay length in the out-of-plane direction, for $\alpha d << 1$, the evanescent wave can reach the opposite interface before it dies off completely (see the field distribution in Au in Figure 1a), interacting with surface polariton at the other interface. In this situation, these two polaritons will combine into a symmetric and an anti-symmetric mode. For each of them, the dispersion is modified from the case of a single interface.

The dispersions for such systems can be obtained from the characteristic equation for a planar waveguide due to structural similarities. Notice that only the fundamental and first order TM mode can be found:[13]

$$\sqrt{\varepsilon_2 k_0^2 - q^2}\, d = \tan^{-1}\left(\frac{\sqrt{q^2 - k_0^2 \varepsilon_1 \varepsilon_2}}{\sqrt{\varepsilon_2 k_0^2 - q^2}\,\varepsilon_1}\right) + \tan^{-1}\left(\frac{\sqrt{q^2 - k_0^2 \varepsilon_3 \varepsilon_2}}{\sqrt{\varepsilon_2 k_0^2 - q^2}\,\varepsilon_3}\right) + m\pi,\ m = 0,1\,. \tag{6}$$

where ε_1 and ε_3 are the permittivities of the upper and lower dielectric media respectively.

If $\varepsilon_1 = \varepsilon_3$, the dispersion relation can be simplified to:

$$\sqrt{\varepsilon_2 k_0^2 - q^2}\, d = 2\tan^{-1}\left(\frac{\sqrt{q^2 - k_0^2\varepsilon_1}\,\varepsilon_2}{\sqrt{\varepsilon_2 k_0^2 - q^2}\,\varepsilon_1}\right) + m\pi,\ m = 0,1 \tag{7}$$

For the Air-Ag-Air structure shown in Figure 1b and 1c, there are two confined mode solutions for **Equation 7**, also at the wavelength of 532 nm. One of them exhibits a symmetric field distribution (m=0), a relatively lower field confinement, and a lower transmission loss, thus it is called long-range surface mode.[14,15] The other one displays an anti-symmetric field distribution (m=1), with higher field confinement as well as transmission loss, therefore it can be called short-range surface mode.

2.1.3. vdW Materials with Negative Permittivity

Due to their layered structure, vdW materials are intrinsically optical anisotropic.[16] Together with the precondition for the existence of polaritons which requires a negative permittivity, vdW materials supporting polaritons may be hyperbolically anisotropic.[17] Take hexagonal boron nitride (h-BN) as an example, let $\varepsilon_\perp$ and $\varepsilon_\parallel$ be the relative permittivities perpendicular and parallel to the optic axis, which is the z axis, respectively.[18] For a specific frequency, the iso-frequency surface in the k-space is given by:[19]

$$\varepsilon_\perp^{-1} k_z^2 + \varepsilon_\mathrm{P}^{-1}(k_x^2 + k_y^2) = (2\pi\omega)^2 \tag{8}$$

When $\varepsilon_\perp$ and $\varepsilon_\parallel$ take opposite signs, the iso-frequency surface is a hyperboloid, which spans to the region where $k_x, k_y \to \infty$, meaning the bulk can support a mode with very large in-plane momentum.

When the in-plane momentum, say k_x is large, the hyperboloid can be approximated by a cone. The ratio between k_x and k_z converges to a fixed value for all large k_x. The direction of group

velocity is perpendicular to such cone or hyperboloid. The angle of the group velocity asymptotically approaches:[19]

$$\tan\theta(\omega) = i\frac{\sqrt{\varepsilon_{\perp}(\omega)}}{\sqrt{\varepsilon_{\parallel}(\omega)}} \tag{9}$$

Which means, the polaritons with high in-plane momentum, will propagate along the same direction. This ray-like propagation behavior of polaritons gives rise to multiple applications such as superlensing.[19,20] Such polaritons can reflect back and forth between the two surfaces of an *h*-BN slab, making *h*-BN an effective waveguide for the hyperbolic phonon polaritons. Taking the out-of-plane anisotropy into account, **Equation 6** should be modified as[21]

$$\sqrt{\frac{\varepsilon_{\perp}}{\varepsilon_{\parallel}}}\sqrt{\varepsilon_{\parallel}k_0^2 - q^2}\,d = \tan^{-1}\left(\frac{\sqrt{q^2 - k_0^2\varepsilon_1}\,\varepsilon_{\perp}}{\sqrt{\frac{\varepsilon_{\perp}}{\varepsilon_{\parallel}}}\sqrt{\varepsilon_{\parallel}k_0^2 - q^2}\,\varepsilon_1}\right) + \tan^{-1}\left(\frac{\sqrt{q^2 - k_0^2\varepsilon_3}\,\varepsilon_{\perp}}{\sqrt{\frac{\varepsilon_{\perp}}{\varepsilon_{\parallel}}}\sqrt{\varepsilon_{\parallel}k_0^2 - q^2}\,\varepsilon_3}\right) + n\pi \tag{10}$$

The in-plane wavevector of hyperbolic polaritons can be very large, and the larger the wavevector the higher the mode order. In Figure 1d we show the second order (n=2) phonon polaritonic mode of a 50-nm-thick *h*-BN slab in the mid-infrared frequency range. Obviously, the field confinement is much higher than those of polaritons in noble metals.

2.2. Origins of Negative Permittivity and Categories of Surface Polaritons

Permittivity encodes the optical response of a material. The larger the permittivity, the larger the material's polarizing capability.[22] In fact, the word "polariton" is coined from the polarization field "particles", analogous to photons.[23] Generally, intrinsic collective modes of material interacting strongly with photons facilitate the origin of negative permittivity, because the Kramers-Kronig relationships usually demand a steep dispersion of the real part of the permittivity, in the vicinity of the collective mode resonance frequency.[24,25] A negative permittivity means the external electric field is screened. Such screening confines the field at the interface and forms surface polariton. Based on the types of the collective modes associated,

polaritons can be classified into surface plasmon polaritons (SPPs),[5] surface phonon polaritons (SPhPs),[26] exciton polaritons (EPs),[27] Cooper pair polaritons,[28] and magnon polaritons,[29] etc. Here we briefly introduce the first three, which have been successfully investigated in the ultrafast-near field experiments.

2.2.1. Plasma Resonance and SPPs

For materials with free charge carriers, the carrier density oscillations can resonate with external field at the plasma frequency ω_p.[30] Without loss of generality, the permittivity of plasmonic systems can be expressed in the Drude form:

$$\varepsilon(\omega) = \varepsilon_\infty \left(1 - \frac{{\omega_p}^2}{\omega^2 + i\gamma\omega}\right) \qquad (11)$$

Where ε_∞ is the high-frequency limit of permittivity, and γ is the damping rate. The plasma frequency is given by $\omega_p = \sqrt{ne^2/(m^*\varepsilon_o)}$. According to **Equation 11**, negative permittivity can be achieved below the plasma frequency, supporting SPPs. The theories, realizations and applications of SPPs can be found in many books and reviews.[5,31-33]

2.2.2. Phonons and SPhPs

Polar materials are usually of permanent dipoles which interact resonantly with mid-infrared light. This resonance constitutes another mechanism of negative permittivity. The frequency-dependent permittivity for polar dielectrics can be expressed as:[34]

$$\varepsilon(\omega) = \varepsilon_\infty \left(1 + \frac{{\omega_{LO}}^2 - {\omega_{TO}}^2}{{\omega_{TO}}^2 - \omega^2 - i\omega\gamma}\right), \qquad (12)$$

where ω_{TO} and ω_{LO} refer to the transverse optical phonon (TO) frequency and longitudinal optical phonon (LO) frequency respectively. According to **Equation 12**, negative permittivity can be realized in the frequency gap between the LO branch and the TO branch, which is known as the Reststrahlen band. The band location and width are determined by the oscillator's

effective mass and the interatomic field strength. As observed in SiC[35,36] and *h*-BN using *s*-SNOM,[37] SPhPs show considerable long lifetime (low damping rate).

2.2.3. Excitons

Exciton, a typical quasiparticle in excited semiconductors, can also couple with photon in proper energy range and forms EPs. Exciton can be regarded as a hydrogen-like system. When the Coulomb interaction between electron and hole is weak, the Wannier excitons with Bohr radius larger than lattice spacing are delocalized and screen out the external electric field. One unique property of exciton polaritons is the spatial dispersion effect because of the non-neglectable ratio of energy transported by excitons. A wavevector-dependent term is included in the dielectric function:[38]

$$\varepsilon(\omega, k) = \omega_\infty \left(1 + \frac{{\omega_L}^2 - {\omega_T}^2}{{\omega_T}^2 - \omega^2 + \beta k^2 - i\omega\gamma}\right) \qquad (13)$$

where $\omega_L$and ω_T are the resonance frequencies of longitudinal exciton and transverse exciton. $\beta = (\hbar\omega_T/M^*)$ where $M^*$is the effective mass of exciton. The *k*-square term introduces more tunable parameters into the dielectric function and results in many unique properties of the EPs. The recent studies have experimentally verified that strong binding exciton can remain stable even in room temperature[39] in Group VI transition-metal dichalcogenides (TMDs) with chemical formula MX_2 (M=Mo, W; X=S, Se).[40-42]

3. Experimental Technique and Polariton Detection

3.1. Near Field Technique

The capability of probing beyond diffraction limit and accessing evanescent waves make *s*-SNOM a promising technique for investigating polaritons.[43] Here we briefly introduce the basic concepts in near-field optics and the *s*-SNOM technique. For a more detailed discussion of modern near-field optical microscopy, readers are directed to several recent reviews.[44-47]

When electromagnetic wave is scattered by an object, the scattered wave always contains both propagating wave and evanescent wave.[48] For evanescent wave, there will be at least one direction, in which the wave vector component is larger than that in free space. A larger wave vector, or a shorter wavelength, can carry information of spatial variations finer than the wavelength of the incident light. On the other hand, the evanescent wave fades away quickly in a distance in the order of wavelengths away from the object surface, therefore undetectable in the far-field.

The detection of evanescent wave is the key to achieve optical imaging beyond the diffraction limit. One method is to put a small probe near the sample surface,[49,50] within the extension of the evanescent field. The probe can act as an antenna and reradiate the evanescent wave to far-field.[50] With the advent of atomic force microscopy (AFM), this idea was developed into many different techniques, one of which is known as *s*-SNOM. The AFM probe, or the "tip", is placed tens of nanometers above the sample surface and polarized by the incident light. The local electric-field beneath the tip apex is greatly enhanced within a range comparable to its radius of curvature *a*. When the tip is brought close to the sample surface, this localized field would interact with the sample strongly. Therefore, the scattered light due to this interaction contains information about the sample volume right beneath the tip. A common practice is to assume the strength of near-field signal as proportional to the localized field between the tip and sample surface, especially in the case of imaging polaritons using *s*-SNOM.

To obtain the genuine near-field signal, the tip-sample separation is modulated by tapping the AFM tip with an amplitude of ~50 nm and a frequency of Ω. The exact tapping amplitude depends on the wavelength of light and the specific setup. Since the near-field signal exhibits strong nonlinearity with the tip-sample distance, it can be effectively extracted by demodulating the output of the detector using a lock-in amplifier at high harmonics of Ω. Due to the signal-to-noise ratio limitation, S_2 or S_3, the second or the third harmonic, are usually chosen.

3.2 Role of *s*-SNOM in Studying Polaritons

Since polaritons are modes confined at sample surface and has an imaginary out-of-plane wave vector, their in-plane momenta are larger than the momentum of light in free space (from **Equation 5**, when ε_1 and ε_2 are of opposite signs, $|q|>|k_0|$.) As a result, direct free space excitation at smooth surfaces cannot yield polaritonic mode. Various methods have been applied to provide extra in-plane momentum. For example, attenuated total reflection (ATR) with dielectric materials is widely used to excite and detect surface polaritons in the far-field experiments.[51-55] The nonlinear excitation[56,57] provides momentum from the nonlinear susceptibility of the material. Gratings[5,58,59] can provide multiples of $g=2\pi/d$ for the in-plane momentum, where d is the spacing of gratings. An artificial metasurface with gradient reflection phase[60] breaks the translational invariance at the interface, thus providing an intrinsic in-plane momentum component at the surface.

Roughly speaking, the tip scattered evanescent wave in a prototypical *s*-SNOM setup spans in a wide momentum range in the order of $1/a$,[61] providing sufficient in-plane momentum for launching polaritons.[62] The tip-launched polaritons spread circularly (as shown in **Figure 2**a) and can be reflected back to the tip by edges or defects of the sample. The total electric field of the incident and reflected polaritons can be picked up by the tip and converted into far-field signal. By scanning the tip across the sample surface, the interference pattern (Figure 2b) between the incident and the reflected polaritons can be registered. For CW laser excitation, the interference pattern comes from a standing wave with alternative nodes and antinodes, where the field amplitude reaches local maxima or minima. The distance between successive antinodes (or nodes) of the standing wave is approximately half of the polariton wavelength.[37,63] In the tip-launched case, the polaritons propagate as cylindrical wave. To comply with the law of conservation of energy, the field strength does not only decay due to the imaginary part of the wave vector, but also with a geometrical factor $1/\sqrt{r}$.

In some cases, the sample edges or other defects can also act as polariton launchers, then the spacing between adjacent signal maxima is approximately one wavelength instead of half wavelength.[64] Also, a straight edge acts as a plane wave source. The decay of edge-launched polariton is purely attributed to the imaginary part of the wavevector. Considering that the tip-launched polaritons travel twice as much as the edge-launched ones, it's easy to understand that, in a system where both integer wavelength and half wavelength are observed, the half-wavelength pattern often decays faster.[64,65]

For *s*-SNOM imaging using ultrafast laser pulses, the imaging mechanism is slightly different. To illustrate the general idea, we divide the imaging process into two steps. The first is shown in Figure 2c. The ultrafast pulse is focused onto the tip apex and induces polaritons. The electric field of the polaritons is picked up by the tip and scattered as a far-field signal into the detector. This far-field signal is labeled as the pink "emitted signal" $E_1(t)$ in Figure 2c. As the emitted signal propagates in the free space, the polaritons propagate as cylindrical wave pulse along the sample surface, denoted as "ultrafast polariton" in Figure 2c.

The second step is shown in Figure 2d. The ultrafast polaritons reach the sample edge, then reflected back. When the reflected polaritons reach the tip, the electric field is picked up by the tip again, converted to another far-field signal, and scattered into the same detector at a later time. Here it's shown as the black "reflected light" in Figure 2d, labeled as $E_2(t)$.

A toy model considers $E_1(t) = E_2(t + \Delta t)$ can be made to illustrate the signal detection here, where Δt is the time for polariton travel from the tip, to the edge, and finally back to the tip. In this model, we ignore all the dispersion, tip-sample coupling, dissipation or phase changes by reflection and capture simply the mechanisms of fringe formation.

At a specific frequency, a Fourier transform of the electric field scattered by the tip shows as:

$$E_1(t) \rightarrow E_1(\omega)$$

$$E_2(t) = E_1(t + \Delta t) \rightarrow E_1(\omega)\exp(i\omega\Delta t)$$

In the frequency domain, they add up as:

$$E_{tot}(\omega) = E_1(\omega) + E_2(\omega) = E_1(\omega)[1 + \exp(i\omega\Delta t)]$$

Again, Δt is the time for polariton to travel back and forth. As the distance between the tip and sample edge changes, the time Δt will change accordingly:

$$\Delta t = 2x/v_p = 2x/(f\lambda_p) = 4\pi x/(\omega\lambda_p)$$

Here v_p, λ_p are velocity and wavelength of the polariton. $f = \omega/2\pi$ is the frequency. The relation $v_p = f\lambda_p$ is used to substitute the velocity. The $2x$ appears due to the total travel distance of the polariton is twice the tip-edge distance. Plug it into the total field:

$$E_{tot}(\omega) = E_1(\omega)[1 + \exp(i\omega\Delta t)] = E_1(\omega)\left[1 + \exp\left(\frac{i\omega 4\pi x}{\omega\lambda_p}\right)\right] = E_1(\omega)\left[1 + \exp\left(\frac{i4\pi x}{\lambda_p}\right)\right]$$

For the phase in the last term to change 2π, the tip-edge distance should change:

$$2\pi = 4\pi x/\lambda_p \Rightarrow x = \lambda_p/2$$

Hence, the spatial periodicity in the detected electric field is half of the polariton wavelength, the same result as in the CW wave experiment. Here, we did not require $E_1(t)$ to be nonzero throughout the time of detection. $E_1(t)$ being an ultrafast pulse or a CW laser does not affect our result. The key for the fringe formation here is that, in a Fourier transform, two pulses with changing intervals between them will result in a changing magnitude at a certain frequency.

For the case of edge-launched polaritons, the travel distance of polaritons is the same as tip-edge distance, so the time delay $\Delta t = x/v_p$, leading to a result of $x = \lambda_p$.

From the discussions above, we can see that, in the ultrafast detection, the polaritons don't have to interfere with themselves to form observable fringes, the distance between adjacent fringes are the same as the CW experiment under the same conditions. This promises that the ultrafast detection of polaritons can share the same modeling as polaritons generated by CW laser.

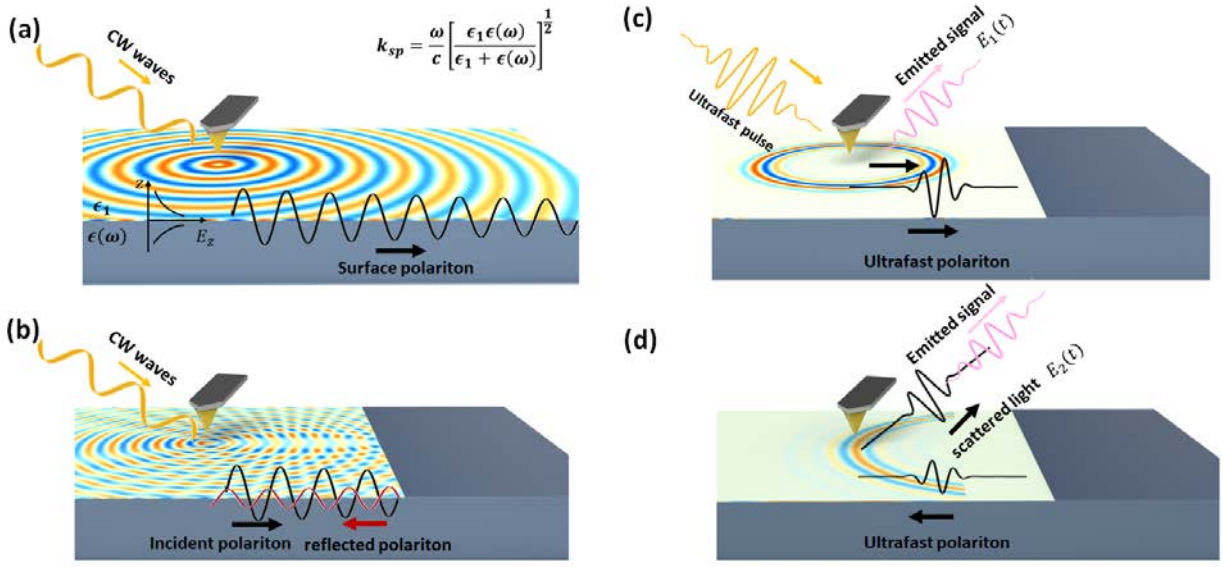

Figure. 2 Polaritons investigated by *s*-SNOM. (a) Surface polariton induced by CW wave with an AFM tip on an interface between dielectric and dispersive material. The CW laser is focused onto the AFM tip, which acts as a point source of the polaritons. The polaritons propagate as cylindrical wave. The color shows the electric field profile. (b) CW polaritons launched by the tip travels from left to right and reflected by the edge. The incident and reflected polaritons superpose and form standing wave. The field profile after interference is picked up by the tip. By scanning the tip, the field strength beneath the tip is recorded. (c) and (d), ultrafast laser-induced polaritons close to the edge of the sample at an early and later time. (c) The ultrafast pulse is focused onto the tip, inducing ultrafast polaritons. The field strength beneath the tip is picked up and scattered, labeled as $E_1(t)$. (d) The ultrafast polaritons reflected by the sample edge reaches the tip again. The scattered light of the reflected ultrafast polaritons by the tip is labeled as $E_2(t)$. Note that, the non-zero part of $E_1(t)$ and $E_2(t)$ may not overlap in space or in time. However, the interference between them can still form periodic patterns, with periodicity the same as the ones in CW induced polaritons under identical conditions. The mechanism is described in detail in the main text.

A realistic experimental setup for near-field detection of CW laser-induced polaritons is shown in **Figure 3**. The whole setup can be split into a light source, an asymmetric Michelson interferometer, a focusing optics and an AFM. The light source produces CW laser, propagates through the beam splitter and is split into a detection arm and a reference arm. The detection arm contains the focusing optics, the AFM and the sample. For a single-wavelength laser, the focusing optics can be a lens. Otherwise, an off-axis parabolic mirror is often used.[44] As the AFM tip raster scans the surface of the sample, the spatial variations in the near-field image suggests the wave vector q in the corresponding laser frequency ω, settling a data point on the dispersion. With tunable laser or various CW light sources, multiple mappings can be done to yield the dispersion relation.

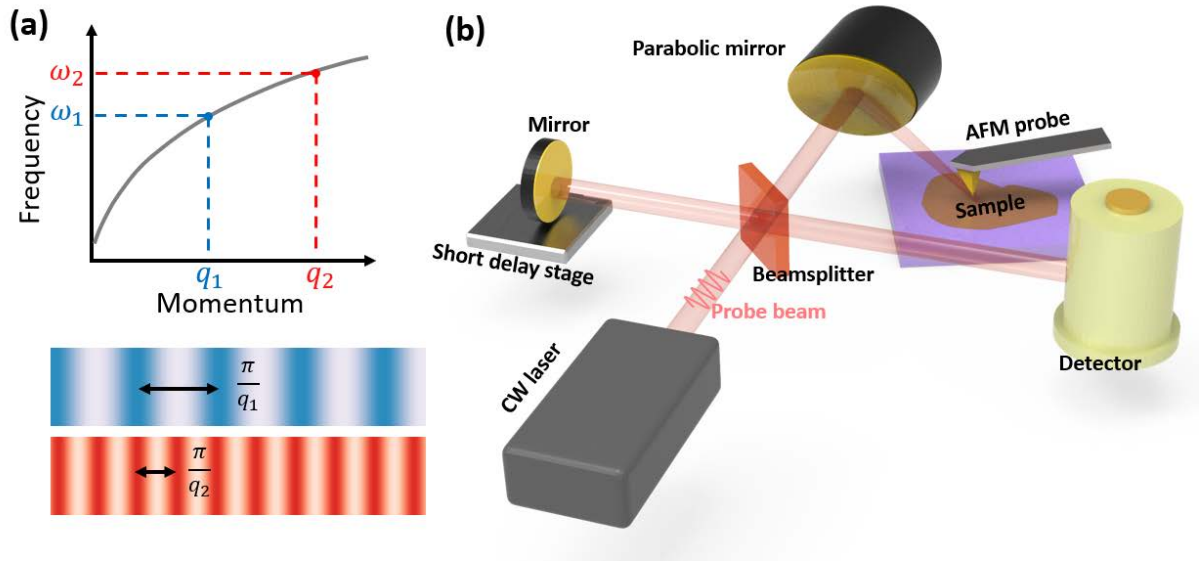

Figure 3 Multi-color mapping of plasmon polariton dispersion using tunable CW lasers. (a) Top panel: schematics of the dispersion relation of plasmon polariton of graphene single-layer on SiO_2. Red and blue cross refer to experimentally extracted data points at two different frequencies. Bottom panel: the interference patterns of tip-launched polaritons corresponding to different frequencies (b). Schematics of the near-field experimental setup.

The case of broadband or time-domain measurements is shown in **Figure 4**. The probe beam is an ultrafast laser rather than CW laser. By moving the reference mirror along a long delay stage, the reference beam can amplify the near-field signal at different time, mapping out the time-profile of the near-field signal. This is similar to the setup of Fourier-transform infrared spectroscopy (FTIR). With a broadband probe light, such as synchrotron light[66] or plasma laser,[67] such setup, so-called nano-FTIR,[68] can measure spectra with a spatial resolution of ~20 nm.[69] Such technique has produced flourish results in phase transition materials,[70-73] polariton dispersion,[74,75] catalytic chemistry,[76] biology,[77] geoscience[78] and various other fields.[79,80]

Another idea for ultrafast measurement is to combine pump-probe setup with *s*-SNOM. A pump light, usually with wavelength shorter than the probe light, is focused onto the tip with the same or different focusing optics with the probe beam. A delay stage is added to the path of the pump beam, to vary the time delay between this two. As the system is pumped away from equilibrium, the dynamics of the system recovering to equilibrium will be detected by the probe beam arriving at various time delays after pumping. The setup has been carried out successfully in the infrared,[81-84] multi-THz[85] and THz[86] frequency regions. This is also the main setup in the detection of ultrafast polaritons using *s*-SNOM. The pseudo-heterodyne detection is also determined to be compatible with the near-field pump probe measurements.[87] However, this method has not been carried out in observing ultrafast polaritons.

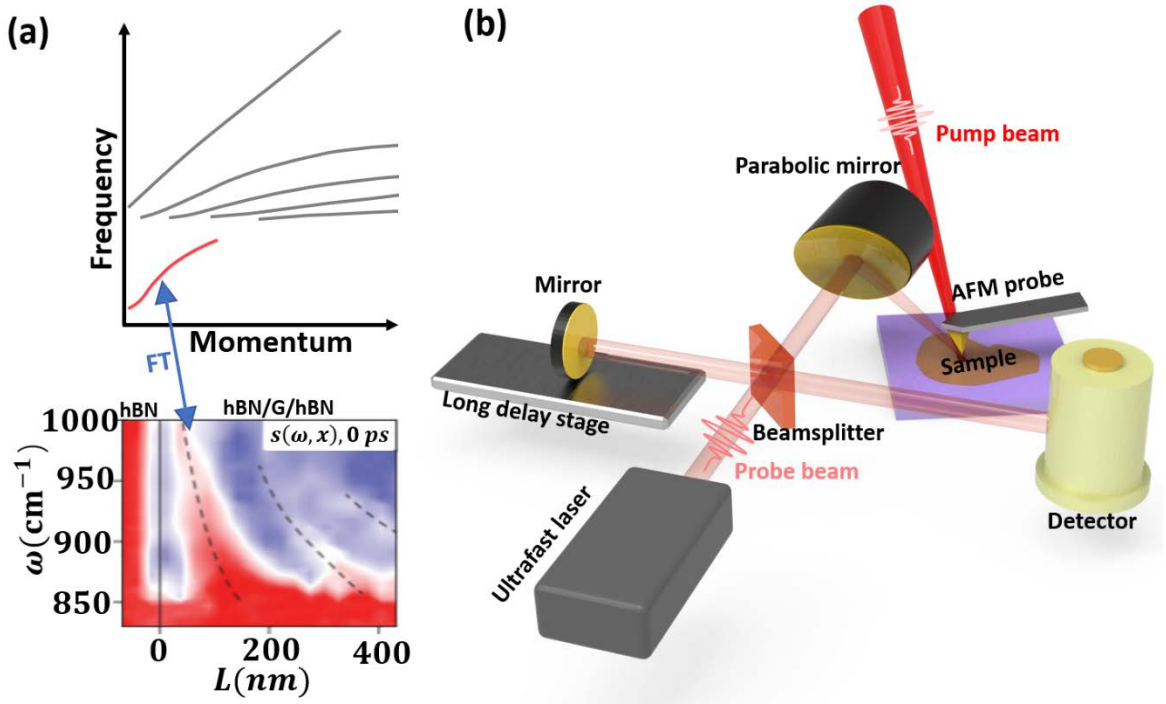

Figure 4 Phonon plasmon polariton dispersion obtained by hyperspectral line scan in an ultrafast broadband near-field setup. (a) Top panel: schematics of the dispersion relation of hybridized phonon-plasmon polaritons of *h*-BN/Graphene/*h*-BN heterostructure Bottom panel: the hyperspectral maps of hybridized phonon-plasmon polaritons in a *h*-BN/graphene/*h*-BN heterostructure with pump-probe delay at 0 fs. (cited from Ref[64]) (b) Schematics of the ultrafast near-field experimental setup.

3.3 Imaging CW Polaritons with *s*-SNOM

Before the near-field experiment on van der Waals materials, graphene plasmons have been widely investigated in the far-field.[88-90] However, the large momentum mismatch between free-space photons and plasmons confined in 2D results in low light-plasmon coupling efficiency in launching and probing of the graphene SPPs. The direct visualization of propagating SPPs in graphene was first achieved by two near-field studies using *s*-SNOM.[63,91] These two works demonstrate that the tapered graphene ribbon on 6H-SiC[91] and graphene/SiO_2/Si back-gate structure[63] can effectively support the propagation of SPPs with highly reduced wavelength ($\lambda_p = \lambda_0/40$). The 2D maps of the near-field amplitude present periodic fringes close to the

graphene edges or defects. These fringes are interpreted as interference between the incident and reflected SPPs, as described in the previous section.

It is noticeable that the line defects play an important role in the formation of the plasmonic interference patterns in real space. Conversely, this nanoimaging is a powerful tool to discover other defects with plasmonic response, for instance, the grain boundaries in graphene prepared by chemical vapor deposition (CVD) [92]. Such boundaries are impossible to observe by AFM but can be characterized by twin fringes in near-field nanoimaging.

Using the Drude-like conductivity model for graphene, the plasmon wave vector can be written as:[63]

$$q_{\mathrm{p}} = \frac{\hbar^2 \kappa(\omega)}{2e^2 E_{\mathrm{F}}} \omega \left(\omega + \frac{i}{\tau}\right) \tag{14}$$

where $\kappa(\omega)$ refers to the effective dielectric function considering the interaction of substrate. E_{F} is the fermi energy and τ is the relaxation time. The plasmon wavelength is determined by the real part of the plasmon wave vector $\lambda_{\mathrm{p}} = \frac{2\pi}{\mathrm{Re}(q_{\mathrm{p}})}$, and the plasmon damping rate is defined as the ratio between the imaginary part and the real part of the wave vector $\gamma_{\mathrm{p}} = \frac{\mathrm{Re}(q_{\mathrm{p}})}{\mathrm{Im}(q_{\mathrm{p}})}$. According to the linear dispersion at two Dirac points in the Brillouin zone, the Fermi momentum can be expressed by the free carrier density in a rather simple form $k_{\mathrm{F}} = \sqrt{\pi|n|}$. By fitting to the line profiles of the interference pattern in experiments, the carrier density and damping rate of plasmon polaritons can be obtained simultaneously.

The electric tuning method is originated from the E_{F} term in Equation (12) which can be electrically controlled by varying the gate voltage.[63,91] As the gate voltage in a p-doped graphene/SiO_2/Si back-gated system decreases, the plasmon wavelength increases and the strength of the interference pattern is enhanced due to increased free-carrier density.[63] Besides the tunability, the quality factor defined as the inverse of the damping rate $Q_{\mathrm{p}} = \frac{1}{\gamma_{\mathrm{p}}}$, is also one of the most important indices for polaritonic devices. Compared with plasmons of noble metals

with high loss due to absorption, graphene plasmons provide promising low-energy loss and long propagation length. In the first near-field experiments, the quality factor measured in graphene/SiO_2/Si structure is unexpectedly low, around 7.4, indicating a rather strong damping rate caused by surface irregularity, enhanced electronic relaxation rate and many-body effects.[63] The later CW imaging of high-quality graphene encapsulated in *h*-BN yields a much higher quality factor valued 50.[93] The damping can also be significantly suppressed in low temperature environment. An unprecedented high quality factor for encapsulated graphene reaches 130 in cryogenic temperature (60K).[94]

A system with strong SPhPs which has been investigated in the near-field regime is *h*-BN, in the form of both nanoflakes and nanotubes.[37,95,96] Fourier transform IR nanospectroscopy (nano-FTIR) was performed to investigate the dispersion of SPhPs in *h*-BN. Compared with the data obtained by the CW imaging, the broadband nanospectroscopy provides an efficient way to map out the dispersion in a single line scan.

The near-field studies on EPs are realised in WSe_2 using aperatured-SNOM[97] and in $MoSe_2$ using *s*-SNOM, respectively.[98] Complex line profiles formed by the interferences of various waveguide modes with different in-plane momenta are observed. The waveguide modes are highly damped when the incident photon energy is larger than the exciton energy. In the $MoSe_2$ waveguides, a long propagation distance of waveguide exciton polariton up to 12 μm was realized.[98]

In a multilayer structure where different types of polaritons coexist, hybridization happens in the vicinity of dispersion crossover. One prototype of the hybrid modes is the phonon-plasmon-polariton.[65,99,100] A strong near-field strength enhancement was investigated in monolayer graphene on SiO_2/Si substrate in 2011.[62] The gate-voltage dependent spectral enhancement around the bare surface optical phonon frequency of SiO_2 is explained by the phonon-plasmon coupling at the graphene-SiO_2 interface. The effect of hybridization strongly relies on the excitation frequency. The hyperbolic phonon polaritons in *h*-BN effectively couple with

plasmon polaritons in graphene, giving rise to the hyperbolic plasmon-phonon polaritons (HPPPs). The HPPPs can be tuned by varying gate voltage but still inherit the low damping rate from hyperbolic phonon polaritons. The propagation length is 1.5-2 times larger than the unhybridized hyperbolic phonon polaritons in *h*-BN. Therefore, HPPPs shows unprecedented features that provide alternative routes to the design and optimization of the polaritonic devices.

3.4 Imaging Ultrafast Polaritons with *s*-SNOM

3.4.1 Spectral measurements

The first near-field imaging of graphene plasmons in 2012 has ignited a worldwide interest in investigating polaritons using *s*-SNOM.[63,91] Up to now, the near-field study of polaritons continued to spur innovation and galvanize thought in a variety of photonics systems that extend to many different research fields[101-104]. Later on, the graphene nanoimaging, and graphene plasmon nanoimaging, has become the touchstone of near-field imaging systems, showing the capabilities of, for example, ultrafast *s*-SNOM,[64,81,105] THz *s*-SNOM[106] and cryogenic *s*-SNOM.[94]

Inspired by the successes of imaging time-independent plasmons excited by CW laser, investigating the plasmon dynamics in the ultrafast regime becomes a natural follow-up. Two years after the original work, infrared pump-probe experiment beyond diffraction limit was first realized in the graphene/SiO_2/Si system (**Figure 5**) with a temporal resolution of ~200 fs.[81] Owing to the fine spatial resolution, especially with the artifact-free methods,[87] the authors in Ref[81] managed to measure the ultrafast electron and lattice dynamics free from interferences from the defects and grain boundaries.

The experiment setup is shown in Figure 5a. The ultrafast (<100 fs) near-infrared (NIR) pulse (λ=1.56 μm) was generated by a 40 MHz Er-doped fiber laser. The MIR probe was generated by difference-frequency mixing of NIR pulse and supercontinuum (SCIR) pulse at λ=1.8 μm in GaSe. The NIR pulse also serves as the optical pump to photoexcite the plasmonic responses, which interact with two phonon modes of SiO_2, α (1125 cm^{-1}) and β (785 cm^{-1}), marked by the

two horizontal lines in Figure 5b. The coupling between the surface phonon in SiO_2 and the plasmons in graphene gives rise to the hybrid phonon-plasmon mode, shown in the calculated dispersion in Figure 5b.

The relative change in near-field amplitude $\Delta s(\omega)/s(\omega)$ increases with the increasing pump power (Figure 5c top). At 10 mW pump power, the pumping effect is similar with a -70 V DC gating. Compared with the peak at high-frequency range (ω >1100 cm^{-1}), the one at the β mode (ω_β =785 cm^{-1}) is wider and more subtle, corresponding to a higher damping and a steeper slope of the plasmon dispersion (Figure 5b). The effect of pumping is explained as an increase of electron temperature. In a previous FTIR spectroscopy measurement of the transmission spectrum of graphene, a Drude-like frequency dependence of conductivity was observed.[107] The conductivity of graphene can be modeled by the following formulas:

$$\sigma(\omega) = \sigma_{\text{intra}}(\omega) + \sigma_{\text{inter}}(\omega), \qquad \sigma_{\text{intra}}(\omega) = \frac{i}{\pi}\frac{D}{\omega + i\gamma}$$

where D is the Drude weight and γ is the scattering rate. The intraband Drude weight

$$D = \left(\frac{2e^2}{\hbar^2}\right) k_B T \ln\left[2\cosh\left(\frac{\mu}{2k_B T}\right)\right]$$

is temperature dependent.[108,109] As $k_B T \gg \mu$, the Drude weight approximately linearly depends on electron temperature. Higher Drude weight increases the slope of plasmon dispersion in graphene, therefore increases the spectral strength of the upper branch (Figure 5b). Meanwhile, larger scattering rate causes the broadening of the dispersion (Figure 5b right). By tuning the Drude weight and scattering rate, the near-field response of the system is modeled in Figure 5c bottom, which shows good agreement with the experiments (Figure 5c top). It is noteworthy that the probe pulse with high in-plane field strength also increases the Drude weight and scattering rate. The plasmonic features in equilibrium state obtained from ultrafast nanospectroscopy is inevitably perturbed by the tip-enhanced probe pulse. Constrained by the limited temporal resolution (200 fs), the fast relaxation process that stems from carrier-carrier

scattering is not accessible but the slower relaxation process is observed in time-resolved changes of spectrally integrated near-field signal (Figure 5d). Two time constants were extracted from the exponential decay, corresponding to the scattering with optical phonon and acoustic phonon respectively. Snapshots of different layers of graphene (Figure 5e) at various time delays confirm the spatial resolution beyond diffraction limit incorporated with sub-picosecond temporal resolution.

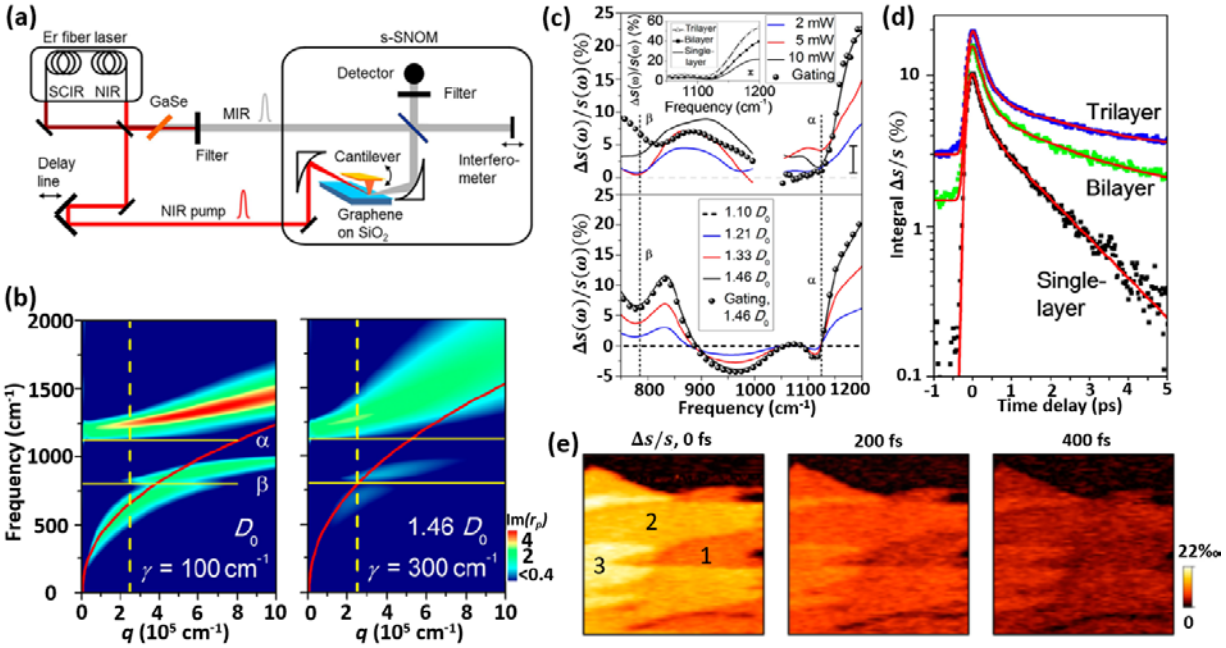

Figure 5 Ultrafast nanospectroscopy of exfoliated graphene (cited from Ref[81]). (a) Schematic of the near-field pump-probe setup. (b) Dispersion relation of phonon-plasmon polariton with different Drude weights D and damping rates γ (left: $D=D_0$, γ=300 cm^{-1}, right: D=1.46 D_0, γ=300 cm^{-1}). (c) Experimental (top) and theoretical (bottom) results of the relative changes in near-field amplitude induced by optical pumping with different power (solid curves) and electrostatic gate (black dots). Two vertical lines β and α correspond to the SiO_2 phonon modes at 785cm^{-1} and 1125 cm^{-1}, respectively. Comparison of the spectral features between pump- and gating-induced data is the first attempt to render insight into the ultrafast plasmon. (d) Time resolved changes of spectrally integrated near-field amplitude $\Delta s/s$ for single-layer, bilayer

and trilayer graphene. (e) $\Delta s/s$ on different layers of graphene at various time delays. The number of graphene layers are shown at the left panel. Area: 6 x 6 μm.

However, the appearance of interference fringes near the sample edge in the CW illumination setup[63] is absent here due to the low carrier mobility and the elevated scattering rate by a factor of 3 at raised electron temperature. To reach the ~200 fs temporal resolution, attenuation achieved by pulse elongation is not applied. As a result, the probe beam heats the electrons to above 1270 K (D=1.10D_0 with MIR probe only) therefore the real-space polariton features are totally damped out.

The first realization of ultrafast near-field response in a narrow bandgap semiconductor using *s*-SNOM is in InAs.[82] The experimental setup is identical to that in Figure 5a. The energy of NIR pump (1560 nm, or 0.794 eV) is larger than the direct bandgap in InAs (0.35 eV). The InAs sample is weakly n-doped so that the equilibrium state does not show any distinct plasmonic feature. The NIR beam pumps electrons into the Γ valley (**Figure 6**d), leading to a higher carrier density before electron-hole recombination. Figure 6a shows near-field amplitude under increasing pump power at 0.8 ps time delay, where the most pronounced changes occurred. A peak appears at the lower frequency end, moves towards higher frequencies and broadened. The changes in peak frequency and width indicates the increase of plasma frequency and scattering rate with increasing pump power. As the pump power increases, the carrier concentration increases accordingly, shifting the plasma frequency into the frequency region available for MIR probe. Figure 6b shows the simulated plot of near-field amplitude with plasma frequency ν_p and scattering rate γ in Drude model. The experimentally retrieved ν_p and γ's are shown in inset of Figure 6b.

The changes in plasma frequency and scattering rate can be mapped out in real time by measuring spectra at different time delays with a fixed pump power (18 mW in Figure 6c). The plasmonic peak appears at ~0.2ps and reaches the highest frequency at 1 ps. The spectral changes in the experiment is well reproduced by Drude model considering the change of plasma

frequency ν_p and scattering rate γ. The retrived dynamics of ν_p and γ shows a ~1 ps raising time, ~1 ps fast decay time and ~60 ps slow decay time, which can be attributed to relaxation of pumped electrons in the Γ valley, carrier-lattice cooling and defect mediated recombination, respectively.[110-112] The evolution of plasma frequency ν_p is shown in Figure 6e.

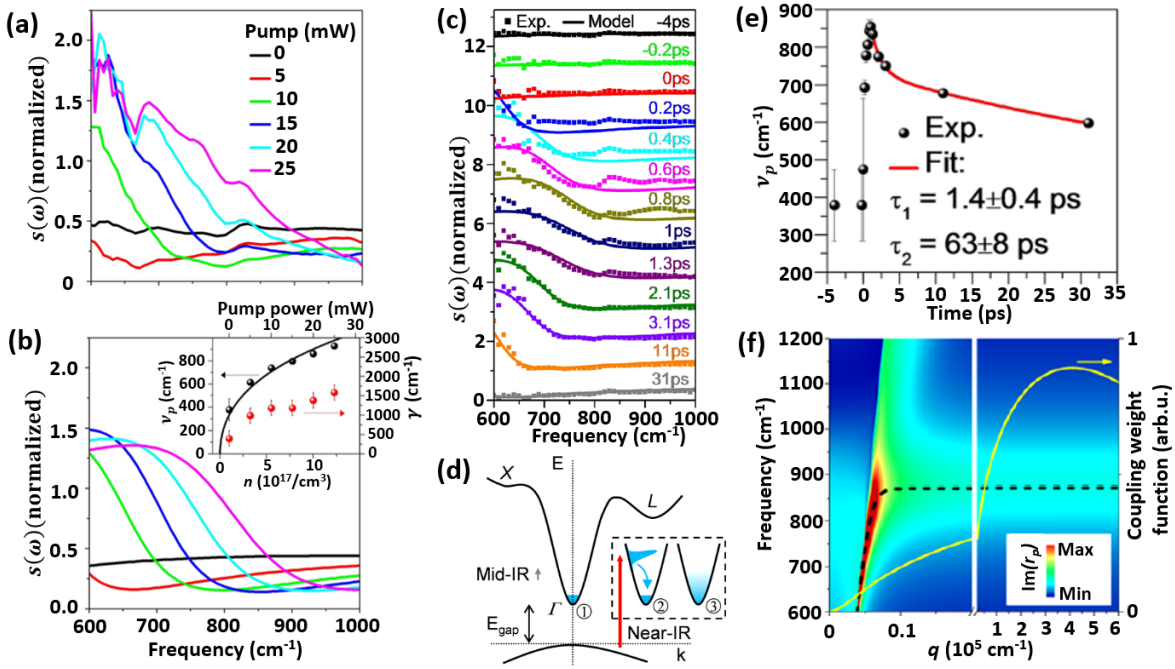

Figure 6 Ultrafast dynamics of surface plasmon in InAs probed by time-resolved infrared spectroscopy (cited from Ref[82]). (a) Near-field spectra with different pump power at 0.8 ps delay time. For photoexcitation power higher than 10 mW, a notable increase of the signal happens at around 650 cm^{-1}. (b) Simulated near-field signal by varying plasma frequency ν_p and scattering rate γ in Drude model. Inset: Change of ν_p and γ with pump power. Dots: experimental data. Black solid curve: modeling results. (c) Time-dependent near-field spectra normalized to gold. Solid curves: modeling results. Dots: experimental data. (d) Band structure of InAs. The energy gap, effect of NIR and MIR pulse are shown. Inset: effect of NIR pulse. Left: nonequilibrium carrier population just after pump. Right: Carrier population after intra-band equilibration, resulted in a Fermi-Dirac distribution with elevated temperature. (e) Bi-exponential fitting of the plasma frequency ν_p with time delays. (f) Plasmon dispersion in InAs.

Color scale shows $\mathrm{Im}(r_p)$. Black dashed curve shows dispersion with negligible scattering as guide to the eyes. Yellow solid curve shows the coupling weight function of a 30 nm tip.

No real-space interference patterns were observed in InAs regardless of the very large time constant (>60 ps) at the plasma frequency. A very important reason is the near-zero group velocity. As shown in Figure 6f, the dispersion for plasmon polariton in InAs is nearly flat at the tip-accessible momentum range (maximum of yellow curve in Figure 6f), implying a near-zero group velocity of plasmon polariton, preventing the polariton propagation. Since the real-space imaging requires interference between incident and reflected polaritons as stated in section (3.2), no interference pattern could be imaged with group velocity almost zero.

3.4.2 Observation of polaritons in real space

To real-space propagation dynamics of plasmon polaritons is observed in high-mobility graphene encapsulated in hexagonal boron nitride (*h*-BN).[64] The dissipation rate of graphene was reduced to ~130 cm^{-1} when being pumped, around one third of the graphene/SiO_2 system. The carrier mobility near the Dirac point exceeds 14,000 cm^2/Vs, larger than that in the graphene/SiO_2 sample with an optimistic estimate result around 10,000 cm^2/Vs.

The experimental setup is shown in **Figure 7**a. High mobility graphene encapsulated in *h*-BN is transferred onto SiO_2 substrate and back-gated. When gated with a voltage of 30 V and pumped with a NIR (1560 nm) ultrafast laser, interference pattern can be observed at the graphene boundary with the help of broadband MIR probe. The plasmon polaritons dispersion can be revealed in a single line scan. In Figure 7c and 7d, the hyperspectral maps at two different time delays show the increase of plasmon wavelength with increasing frequency, which agrees well with the calculated plasmon dispersion (Figure 7e). The plasmonic response is the strongest at the zero-time delay, showing 3 observable interference fringes. At the 2 ps time delay, the response diminishes, and only 1 fringe is observable. The wavelength at the same frequency ω also decreases.

By comparing the ultrafast results (Figure 7c and d) with interference pattern under 890 cm^{-1} CW laser, the spacings between the adjacent fringes are determined as λ_p instead of $\lambda_p/2$. The authors proposed it's due to the charge accumulation at the boundary that excites the in-plane dipole moment of the tip.

By counting λ_{p}, a set of frequency-wavelength relations can be obtained. The effective electron temperature and Drude weight can be determined via model fitting. The relation between plasmon wavelength and Drude weight is given by:

$$\lambda_{\mathrm{p}} = 4\pi D(T_{\mathrm{el}})/\kappa(\omega)\omega^2$$

Where $D(T)$ is the Drude weight in graphene and κ is the permittivity of *h*-BN. As D decreases, the plasmon wavelength decreases, which is clearly observed by comparing Figure 7c to 7d. In Figure 7c, the effective electron temperature T_{el} is 3200 K at zero time delay. As the electron temperature drops with increasing time delay, the Drude weight decreases and leads to a smaller wavelength at the same frequency, as shown in Figure 7d, where T_{el}=1700 K.

The authors proposed a transient process in which carriers follow a non-Fermi-Dirac distribution immediately after the pumping, followed by two separate Fermi-Dirac distributions for electrons and holes with nearly equal and very high temperature T_{el} but different chemical potentials. The chemical potentials equilibrate at a later time, then T_{el} gradually approaches that of the lattice. However, due to insufficient temporal resolution, these dynamics, especially the first two transient processes, were not directly probed by this work. The real-space plasmon polariton propagation as a function of time is also not observable due to the limited temporal resolution.

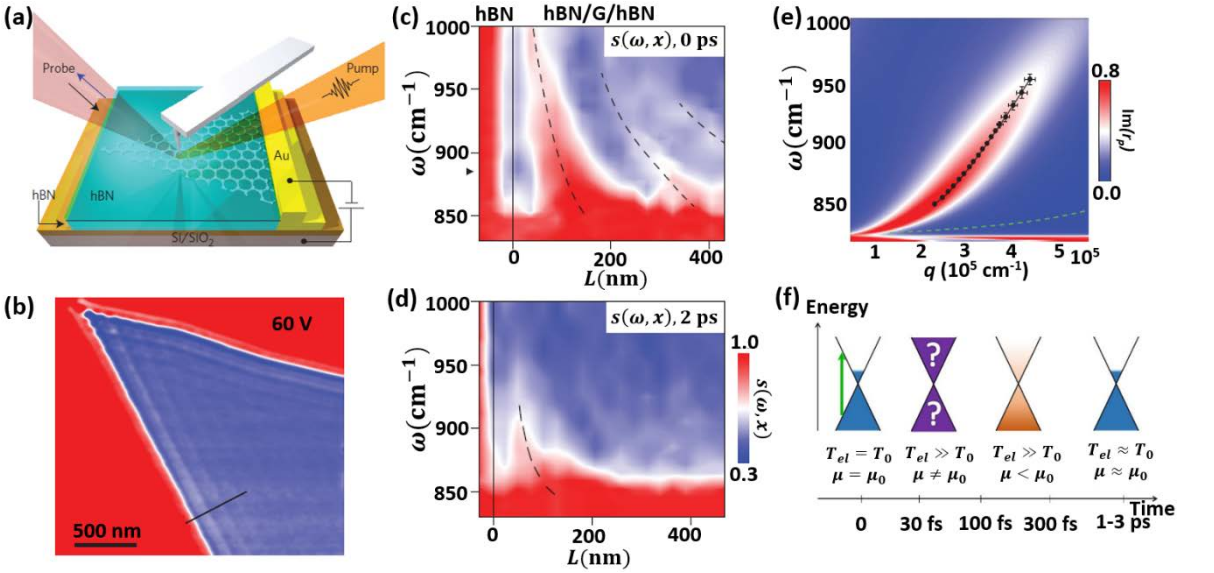

Figure 7 Ultrafast optical switching of infrared plasmon polaritons in high-mobility graphene (cited from Ref[64]). (a) Schematics of the pump-probe nano-IR near-field setup and the *h*-BN/graphene/*h*-BN heterostructure with gating. (b) Plasmon interference pattern obtained using a 890 cm^{-1} CW laser with 60 V gating. (c) and (d) Hyperspectral line scans in photo-excited *h*-BN/graphene/*h*-BN heterostructure at 0 time delay and 2 ps time delay, respectively. (e) Theoretical results (color) and experimental data (black dots) of the dispersion at T_{el}=3200 K and $\gamma_p = 0.15$. (f) Schematic evolution of the carrier population dynamics in graphene, following photo excitation.

Experiments of encapsulated graphene revealed a mechanism of edge-launched polaritons and the capability of observing ultrafast polariton dynamics using near-field setup.

Encapsulated BP shows relatively low near-field signal compared with the SiO_2 substrate without pumping (**Figure 8a** top). When pumped by a 1560 nm, 40 fs NIR beam, the near-field signal increased substantially, and shows alternative bright and dark fringes parallel to the sample edge (Figure 8a bottom), which is similar to the aforementioned interference pattern of SPPs or SPhPs observed in CW based near-field experiments.

To determine the origin of the near-field pattern, the polariton dispersions of BP/SiO_2 heterostructure are derived under unpumped and pumped conditions (Figure 8c). The SPhPs of

SiO_2 splits into two branches due to the coupling between two interfaces of cover layer SiO_2. The lower frequency longitudinal optical mode is labeled as LO-. Similarly, the SPP mode of BP splits due to the coupling between two BP/SiO_2 interfaces, into a symmetric (asymmetric) mode with lower (higher) energy, SPP- (SPP+). Without pump, LO- and SPP+ stay uncoupled (Figure 8c left). When pumped by NIR pulse, electron-hole pairs will be excited, raising the carrier density, as well as the plasma frequency ν_p. When ν_p is raised to the Reststrahlen band (between two horizontal white dashed lines in Figure 8c), SPP+ and LO- will intersect, forming hybrid modes. The right panel of Figure 8c shows the hybrid mode of SPP+ and LO- in the white circle when ν_p=38 THz, which resides in the Reststrahlen band of SiO_2. Compared with SPPs, SPhPs are endowed with low optical loss but poor tunability. However, the hybridization of SPPs and SPhPs in BP seems to overcome this drawback.

A line scan across the SiO_2/BP heterostructure boundary was done to obtain the dispersion relation for comparison with theoretical predictions. The hyperspectral map of this line scan is shown in Figure 8d. The wavelength doesn't change much with the frequency. By imposing Fourier transform for each frequency on Figure 8d, the dispersion of the hybrid polaritons can be obtained, as shown in Figure 8e. The polariton response is confined in the hybrid region of SPP+ of BP and LO- of SiO_2. Two vertical dashed lines show the minimum momentum resolution limited by the total length of the line scan. The theoretical dispersion in the same frequency-momentum region is shown in Figure 8f with ν_p=36.6 THz for comparison.

To investigate the time evolution of plasmon-phonon polaritons, line scans at different time delays are performed. The results are shown Figure 8b left panel. Fitting sine curves to each line scan produces the evolution of polariton strength as shown in Figure 8b right panel. Thus, the rise time for the polariton response to reach half of its maximum is determined to be within 90 fs. It can also be observed that, the wavelength doesn't change much with time delay, meaning the wavelength of hybrid polariton only weakly depends on the carrier density or

plasma frequency. The hybrid polariton response is relatively decoupled with pump photon energy or carrier density, occupying a region selected by the intersection in frequency-momentum space during the entire ~5 ps lifetime of the hybrid polaritons. The line profiles in experiment also show good agreement with damping-free propagation theoretical calculation, indicating low damping rate for the hybrid polariton, which resembles the phonon-like nature stated in section (2.2.2).

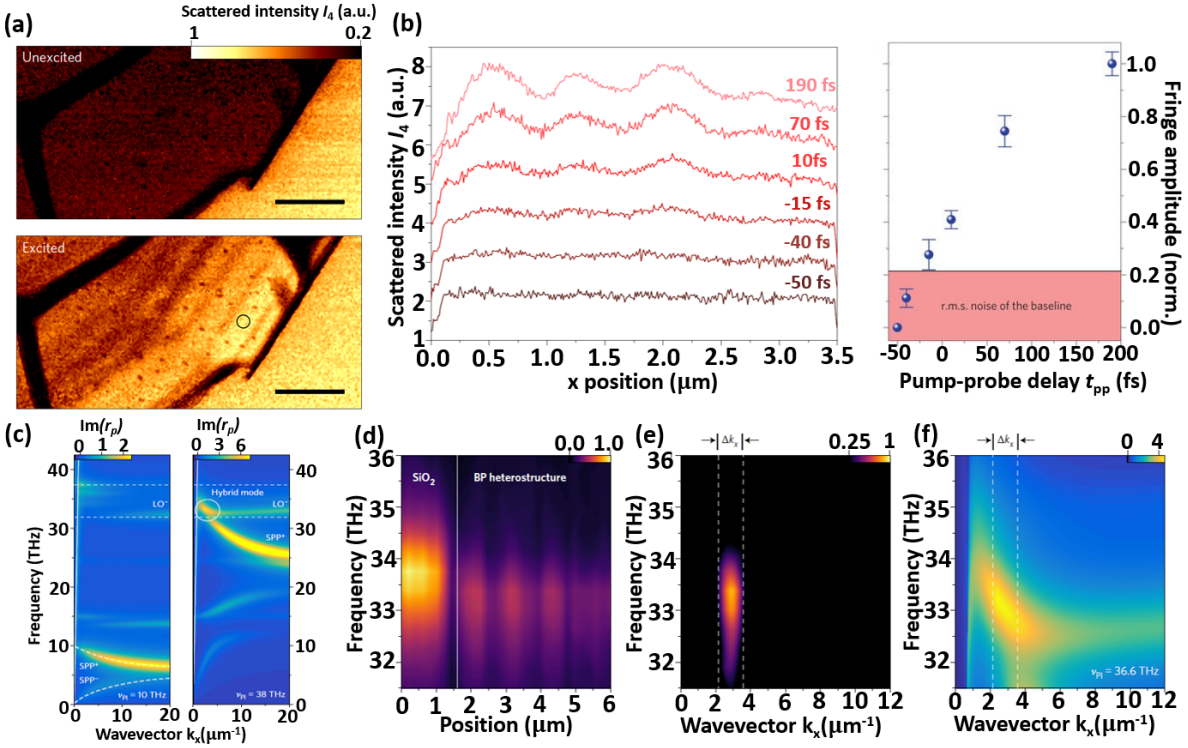

Figure 8 Femtosecond photo-switching of interface polaritons in black phosphorus heterostructures (cited from Ref[65]). (a) Near-field amplitude I_4 before (top) and 250 fs after (bottom) pumping. SiO_2/BP/ SiO_2 heterostructure sample is at left and SiO_2 substrate at right. The interference fringes parallel to the sample boundary are clearly seen. Scale bar: 2 μm. (b) Left panel: Near-field line scans at different time delays across the sample boundary. Right panel: Dependence of average interference amplitude on time delay. (c) Calculated dispersion of BP polaritons with plasma frequency at 10 THz (left) and 38 THz (right), corresponding to unpumped and pumped status respectively. SiO_2 Reststrahlen band sits between the two white dashed lines. (d) Hyperspectral line scan in the direction perpendicular to the stripes. (e) The

dispersion of hybrid phonon-plasmon polaritons, obtained by Fourier transform in *x*-direction of Figure 8d. (f) Theoretical dispersion with plasma frequency at 36.6 THz. The same frequency-momentum region in e is labeled by a circle.

3.4.3 Spatiotemporal imaging

The real-space imaging of polaritons directly revealed the electric field profiles in a sub-wavelength scale, utilizing the high spatial resolution capability of *s*-SNOM. However, due to the limited temporal resolution and high damping, one is unable to obtain useful information such as the group or phase velocity. Recently, in the visible-near-infrared (VIS-NIR) frequency range, the temporal and spatial resolution of near-field pump-probe system has achieved 43 fs and 50 nm respectively, allowing the first direct spatiotemporal imaging of exciton polariton (EP) in a WSe_2 slab, and revealing its group velocity to be v_g~0.017c.[113]

The experiment setup is shown in **Figure 9**a. A sub-10 fs broadband Ti:Sapphire laser beam is split into pump (650-700 nm) and probe (700-1050 nm) beams by a dichroic mirror (DM). The temporal resolution is determined by the convolution between the pump and probe to be ~ 43 fs. The near-field images are obtained at the wavelength of 760 nm, close to the A exciton transition in WSe_2 (inset of Figure 9a) thus show strong near-field signal contrast.

The snapshots of interference patterns at different time delays are shown in Figure 9b. The number of interference fringes is increasing with time. Figure 9c shows the result of spatiotemporal imaging, where the line profile of the polariton fringes is plotted versus time (inset shows the real-space image and the linescan). With increasing time delay, the first stripe moves inward (to the left in Figure 9c) and new stripes appear at the right boundary. The right triangle shows the distance Δx the first stripe has moved within a time interval Δt, yielding an estimation of the group velocity ~ $4.7 \pm 0.5 \times 10^6$ m/s.

The observed pattern was determined to be the "constructive interferences of the EP wave packets propagating inside WSe_2 slab waveguide". The loss of EP wave packet was estimated to be ~2.6 μm^{-1}, which is likely caused by collisions between EP and photo-injected free

electrons. In this work, the modification of the dielectric function introduced by intense laser around the exciton resonance,[114] so called "renormalization", was realised in WSe_2. The renormalization was a 40-80 meV splitting between longitudinal exciton and the corresponding transverse exciton, which is large comparing to the typical value of 2 to 3 meV caused by exciton-light coupling in bulk semiconductors.[115] The large renormalization, being the cause of slow EP group velocity, is a manifestation of the growing strong Coulomb interaction in TMD-layered material as they are thinned down.

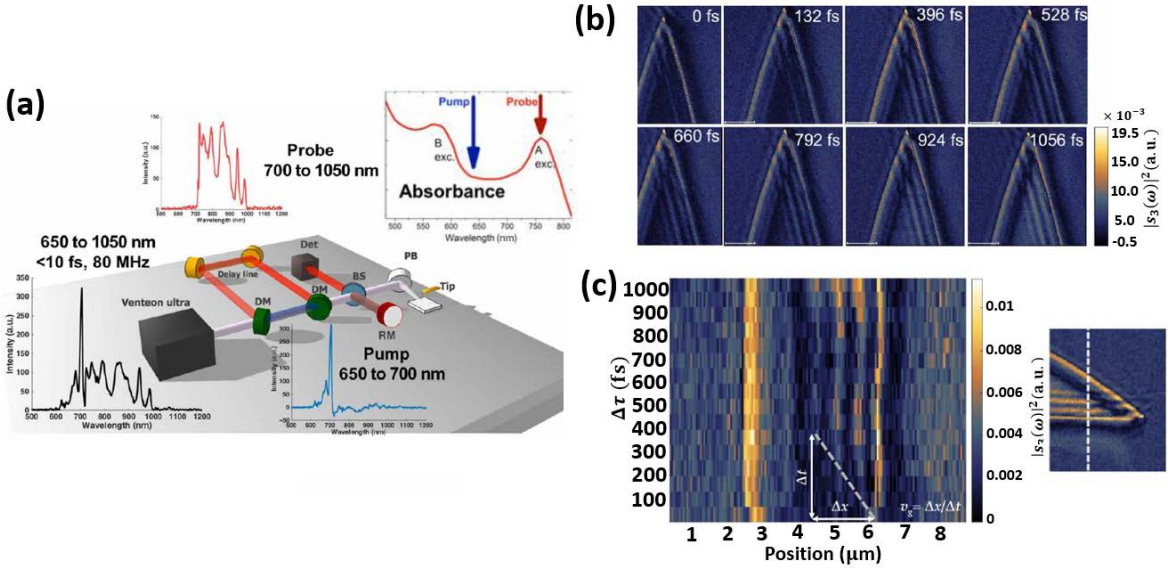

Figure 9 Ultrafast exciton polaritons in a WSe_2 flake (cited from Ref[113]). (a) Schematics of the ultrafast near-field setup. The laser beam was split into broadband pump (500 nm to 700 nm) and probe (700 nm to 1050 nm). The spectra of the 10 fs Ti:Sapphire beam, the pump beam and the probe beam are shown. Inset: absorbance spectra of WSe_2 slab. Two exciton resonance A and B are shown together with the wavelength of pump and probe beam. (b). Snapshots of near field signal intensity $|S_3|^2$ with different time delays on WSe_2 wedge. (c) Line profile of exciton polariton (horizontal axis) with different delay time (vertical axis). The onset of the exciton fringe is shown as the white dashed line. The group velocity can be estimated by the right triangle, which illustrate the distance Δx the fringe has moved in time Δt.

The ultrafast near-field measurements of phonon polariton in *h*-BN by Yoxall et al.[116] reveals a propagation mode with negative phase-velocity and a group velocity down to 0.002*c* using ~100fs pulses. In a homodyne scheme (**Figure 10**a), $E_{\mathrm{ref}}E_{\mathrm{nf}}$[44] i.e. the multiplication of reference with the near-field signal is measured. The reference beam amplifies the near-field signal and provide a time-resolved measurement, yielding the time profile of the electric field of polaritons. In this setup, polaritons are launched by the edge of gold film, propagate in a *h*-BN slab, and picked up by the AFM tip. By a line scan across the gold edge, a 2D mapping of signal intensity with respect to position and delay time τ can be obtained (Figure 10c). When τ is close to 0, the bright fringes show the light scattered directly from the tip (E_{dir}). As τ increases, the hyperbolic polaritons that reach the tip can be observed (E_{HP}). A 2D Fourier transform of Figure 10c produces the frequency-momentum relation. Figure 10d is the 2D FT of one of the position-time delay mappings, in which the fundamental hyperbolic polaritonic mode (M_0) are shown with other modes. From the dispersion, it can be observed that, the group velocity, $\partial\omega/\partial|k|$, is negative. Figure 10d is the real part of the inverse 2D Fourier transform of the modified dispersion with only M_0 saved by applying a Hanning window filtering out all other modes. A clear wave packet propagation from gold edge is shown. The inset is a zoom-in of the wave packet. While the wave packet travel from top-left to bottom-right in the figure, the equal-phase line moves from bottom-left to top-right. That is to say, the phase velocity and the group velocity travel in opposite directions. This opposite motion can further be corroborated by the right panel of Figure 10d, which are several succeeding time slices in the left panel.

It is worth noting that the slow group velocity down to 0.002*c* and the negative phase velocity only appear in one of the two hyperbolic frequency regions of *h*-BN. The one with negative phase velocity, HPI, is found between 760 and 825 cm^{-1}. There is also HPII, found in 1370 and 1610 cm^{-1}, has group velocity ~0.027*c* and positive phase velocity. Figure 10c is a position-time mapping of HPII.

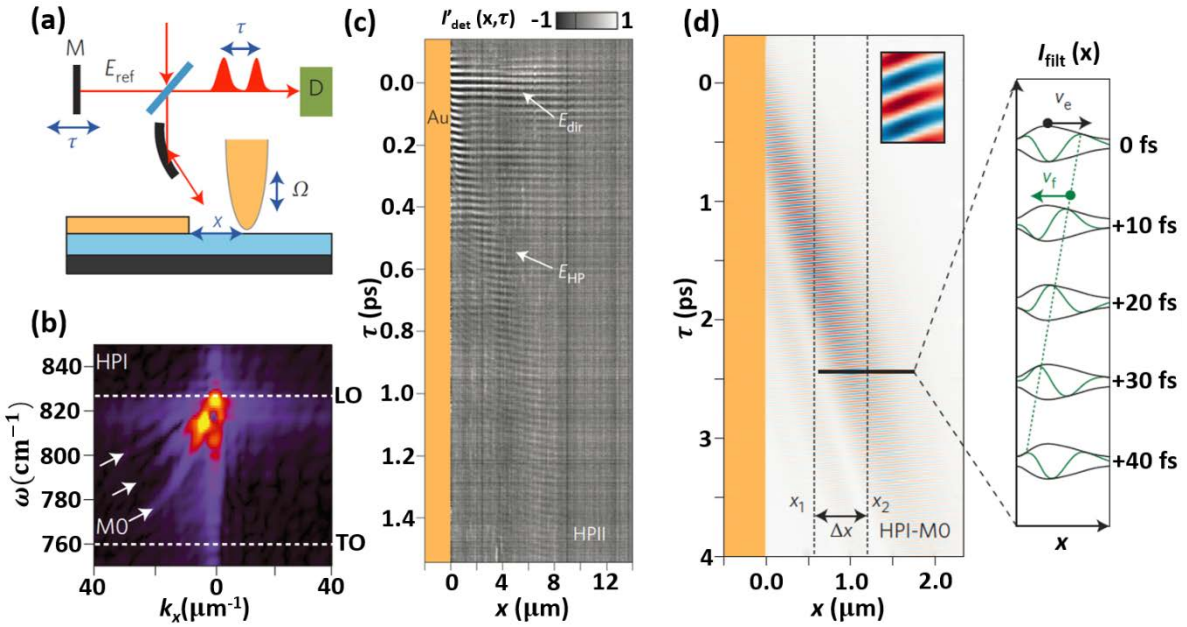

Figure 10 Real-time imaging of hyperbolic phonon polaritons in *h*-BN (cited from Ref[116]). (a) Experimental setup. The incident ultrafast (~100 fs) pulse is split into detection and reference arm. The time delay τ between the two paths is adjusted by moving the reference mirror M. (b) Dispersion of type-I hyperbolic phonon polaritons (HPI). The fundamental mode M_0 is the most distinct. Other modes can also be seen. (c) Position-time mapping by combining line scans across the gold-sample boundary at different time delays. The field directly scattered from the tip E_{dir} and the field from HPII E_{HP} are observed. (d) Real time field profile of filtered dispersion, saving only M_0 branch in (b). The wave packet travel from top-left to bottom-right, while the phase (inset) travel in the opposite direction. The right panel shows the field profile moves in the opposite direction of the envelope, showing a negative phase velocity.

4. Outlook

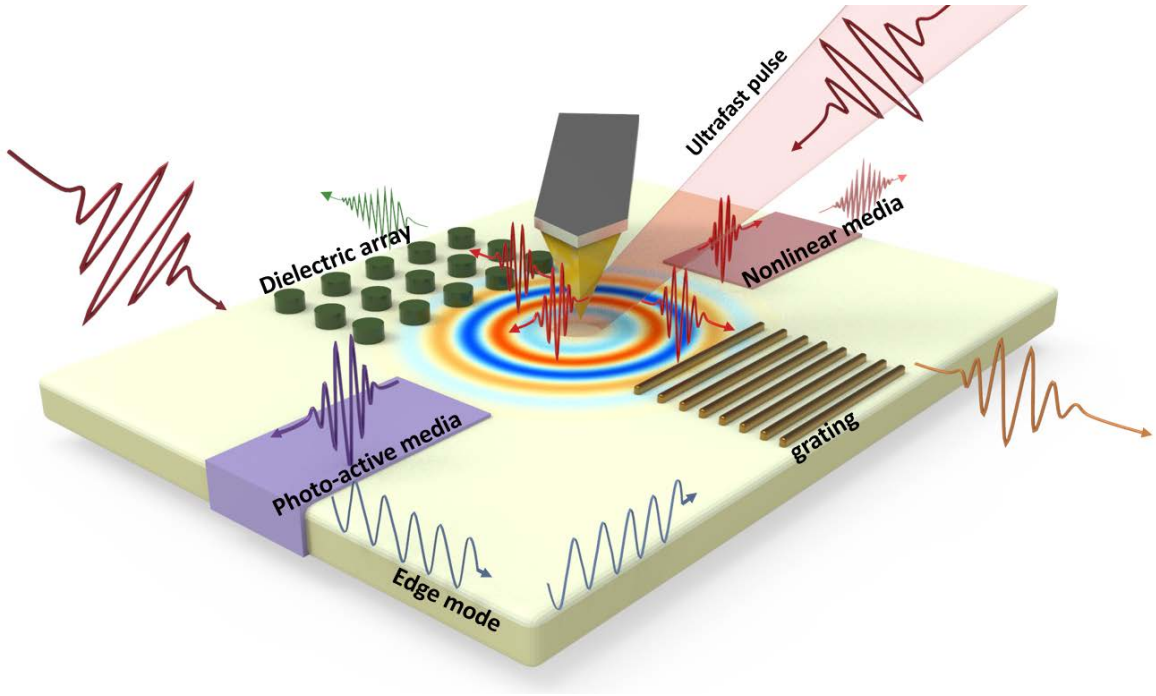

Figure 11 Schematics of future developments and applications in ultrafast near-field polariton detection. The "lab-on-chip" idea is shown as the combination of exotic materials and structures as sources, modulators or detectors onto single device. Possible developments shown here include the following possibilities: photonic crystals with local doping by dielectric arrays, chiral edge mode by effective spin-orbit coupling, polariton loss compensation by photo-active media, light emission control by gratings, and mode conversion with nonlinear media. See main text for a thorough description.

In this report, we have reviewed recent progress on ultrafast near-field characterization of polaritonic materials. Still a nascent field, ultrafast near-field nano-optics has already demonstrated exceptional ability to investigate time-resolved phenomenon at fundamental time and length scales of polaritonic excitations. Here we underscore important current trends that may lead to the advances of future ultrafast plasmonic, or more generally, polaritonic circuits. We also conclude the important challenges that remain to be addressed in the field of *s*-SNOM.

1. The realization of the "lab-on-chip" experiments of polaritonic circuits is within reach. For example, a plasmonic circuit[117] where sources, modulators, and detectors are integrated

into a single chip will yield a compact experimental layout. Tip launched or detected polaritonic waves can serve as a key component for exciting or probing the local element to facilitate the design phase. This idea is schematically illustrated in Figure 11.

2. Concept of photonic crystals,[118] metamaterials,[99] metasurfaces,[119] and recently proposed moiré photonic architectures[120] can be incorporated into the polaritonic chip. Polariton waves modulated via photonic bandgap engineering or subdiffractional metallic composites can enable many intriguing functionalities such as and extraordinary optical transmission, light trapping in thin film solar cells.

3. Artificial induced TM-TE mode splitting as effective spin-orbit coupling,[121] where one-way propagating edge modes can be constructed. Combined with new chiral phenomenon which predicted to be non-dissipative, the low dissipation, chiral polaritons[122,123] can yield important quantum phenomenon such spin-dependent polariton–polariton interaction.

4. The loss in polaritonics can in principle be compensated by parametric amplification,[124,125] photo-active, plasmonic cavities or optical gain media.[126,127] For example, integrated quantum wells with gain-enhanced antenna structures enables sustained polaritonic on-chip with sub-diffraction.

5. Grating structure, or metamaterial antennas[128] which direct light and control the re-emission will serve as important modulation methods for ultrafast electronics. For example, fast scanning of the laser beam using electrical means can be utilized to redirect or reshape of the beam profile, where the control of group velocity and phase front play a pivotal role.

6. Nonlinear media[129] or mode conversion can modify low group velocities, which are required for sensitive spectroscopy and nonlinear light conversion.

In conclusion, the ultrafast near-field detection setup can be combined with multiple materials or structures. This combination can provide platform for a more thorough study of polaritons, on their spatiotemporal behaviors with finer resolutions and broader tenability. New approaches

to and applications of light manipulations via various polaritons can also be expected. Being a nascent field, ultrafast near-field polaritons show great potentials in exploring the nano world.

Acknowledgements
The authors thank Alexander S. McLeod, Wenjie Wang (Ithatron Optics), Andrea Huber (Neaspec, Inc.), G. Lawrence Carr, Hans A. Bechtel, Michael Martin, Haidan Wen, S. T Chui, and Gregory O. Andreev for their helpful discussions. Q.D. and D.H. thank the support from the National Basic Key Research Program of China (No. 2015CB9324000) and the National Natural Science Foundation of China (No. 11704085).

Received: ((will be filled in by the editorial staff))
Revised: ((will be filled in by the editorial staff))
Published online: ((will be filled in by the editorial staff))

References:

[1] D. N. Basov, M. M. Fogler, F. J. García De Abajo, *SCIENCE* **2016**, *354*, g1992.

[2] T. Low, A. Chaves, J. D. Caldwell, A. Kumar, N. X. Fang, P. Avouris, T. F. Heinz, F. Guinea, L. Martin-Moreno, F. Koppens, *NAT MATER* **2017**, *16*, 182.

[3] E. Burstein, W. P. Chen, Y. J. Chen, A. Hartstein, *J Vac Sci Technol* **1974**, *11*, 1004.

[4] D. L. Mills, E. BURSTEIN, *REP PROG PHYS* **1974**, *37*, 817.

[5] H. Raether, *Surface Plasmons on Smooth and Rough Surfaces and on Gratings*, Springer, Berlin **1988**.

[6] A. Amo, T. C. H. Liew, C. Adrados, R. Houdré, E. Giacobino, A. V. Kavokin, A. Bramati, *NAT PHOTONICS* **2010**, *4*, 361.

[7] A. Vakil, N. Engheta, *SCIENCE* **2011**, *332*, 1291.

[8] D. Rodrigo, O. Limaj, D. Janner, D. Etezadi, F. J. García De Abajo, V. Pruneri, H. Altug, *SCIENCE* **2015**, *349*, 165.

[9] D. Rodrigo, A. Tittl, N. Ait-Bouziad, A. John-Herpin, O. Limaj, C. Kelly, D. Yoo, N. J. Wittenberg, S. Oh, H. A. Lashuel, H. Altug, *NAT COMMUN* **2018**, *9*, 2160.

[10] I. Lee, D. Yoo, P. Avouris, T. Low, S. Oh, *NAT NANOTECHNOL* **2019**, *14*, 313.

[11] P. R. West, S. Ishii, G. V. Naik, N. K. Emani, V. M. Shalaev, A. Boltasseva, *LASER PHOTONICS REV* **2010**, *4*, 795.

[12] M. Born, E. Wolf, *Principles of Optics*, Cambridge University Press, Cambridge, U.K. **1999**.

[13] K. Kawano, T. Kitoh, *Introduction to Optical Waveguide Analysis*, John Wiley & Sons, New York **2001**.

[14] D. Sarid, *PHYS REV LETT* **1981**, *47*, 1927.

[15] P. Berini, *ADV OPT PHOTONICS* **2009**, *1*, 484.

[16] Y. L. W, *J Phys C: Solid State Phys* **1973**, *6*, 551.

[17] E. E. Narimanov, A. V. Kildishev, *NAT PHOTONICS* **2015**, *9*, 214.

[18] A. Poddubny, I. Iorsh, P. Belov, Y. Kivshar, *NAT PHOTONICS* **2013**, *7*, 948.

[19] S. Dai, Q. Ma, T. Andersen, A. S. Mcleod, Z. Fei, M. K. Liu, M. Wagner, K. Watanabe, T. Taniguchi, M. Thiemens, F. Keilmann, P. Jarillo-Herrero, M. M. Fogler, D. N. Basov, *NAT COMMUN* **2015**, *6*, 6963.

[20] P. Li, M. Lewin, A. V. Kretinin, J. D. Caldwell, K. S. Novoselov, T. Taniguchi, K. Watanabe, F. Gaussmann, T. Taubner, *NAT COMMUN* **2015**, *6*, 7507.

[21] D. Hu, X. Yang, C. Li, R. Liu, Z. Yao, H. Hu, S. N. G. Corder, J. Chen, Z. Sun, M. Liu, Q. Dai, *NAT COMMUN* **2017**, *8*, 1471.

[22] R. E. Newnham, *Properties of materials: anisotropy, symmetry, structure*, Oxford University Press, Oxford **2005**.

[23] J. J. Hopfield, *Phys Rev* **1958**, *112*, 1555.

[24] J. S. Toll, *Phys Rev* **1956**, *104*, 1760.

[25] V. Lucarini, K. Peiponen, J. J. Saarinen, E. M. Vartiainen, *Kramers-Kronig Relations in Optical Materials Research*, Springer, **2005**.

[26] G. Borstel, H. J. Falge, *Phys Status Solidi B* **1977**, *83*, 11.

[27] L. Schultheis, J. Lagois, *SOLID STATE COMMUN* **1982**, *44*, 1557.

[28] H. T. Stinson, J. S. Wu, B. Y. Jiang, Z. Fei, A. S. Rodin, B. C. Chapler, A. S. McLeod, A. Castro Neto, Y. S. Lee, M. M. Fogler, D. N. Basov, *PHYS REV B* **2014**, *90*, 14502.

[29] J. Matsuura, M. Fukui, O. Tada, *SOLID STATE COMMUN* **1983**, *45*, 157.

[30] L. Tonks, I. Langmuir, *Phys Rev* **1929**, *34*, 876.

[31] S. Kawata, *Near-Field Optics and Surface Plasmon Polaritons*, Springer, Berlin **2001**.

[32] W. L. Barnes, A. Dereux, T. W. Ebbesen, *NATURE* **2003**, *424*, 824.

[33] A. V. Zayats, I. I. Smolyaninov, A. A. Maradudin, *Phys Rep* **2005**, *408*, 131.

[34] J. D. Caldwell, L. Lindsay, V. Giannini, I. Vurgaftman, T. L. Reinecke, S. A. Maier, O. J. Glembocki, *NANOPHOTONICS-BERLIN* **2015**, *4*, 44.

[35] R. Hillenbrand, T. Taubner, F. Keilmann, *NATURE* **2002**, *418*, 159.

[36] D. V. Kazantsev, *JETP Lett* **2006**, *83*, 323.

[37] S. Dai, Z. Fei, Q. Ma, A. S. Rodin, M. Wagner, A. S. McLeod, M. K. Liu, W. Gannett, W. Regan, K. Watanabe, T. Taniguchi, M. Thiemens, G. Dominguez, A. H. C. Neto, A. Zettl, F. Keilmann, P. Jarillo-Herrero, M. M. Fogler, D. N. Basov, *SCIENCE* **2014**, *343*, 1125.

[38] J. J. Hopfield, D. G. Thomas, *Phys Rev* **1963**, *132*, 563.

[39] Z. Ye, T. Cao, K. O Brien, H. Zhu, X. Yin, Y. Wang, S. G. Louie, X. Zhang, *NATURE* **2014**, *513*, 214.

[40] X. Liu, T. Galfsky, Z. Sun, F. Xia, E. Lin, Y. Lee, S. Kéna-Cohen, V. M. Menon, *NAT PHOTONICS* **2014**, *9*, 30.

[41] X. Liu, W. Bao, Q. Li, C. Ropp, Y. Wang, X. Zhang, *PHYS REV LETT* **2017**, *119*, 27403.

[42] Y. Chen, J. D. Cain, T. K. Stanev, V. P. Dravid, N. P. Stern, *NAT PHOTONICS* **2017**, *11*, 431.

[43] B. Knoll, F. Keilmann, *J Microsc* **1999**, *194*, 512.

[44] X. Chen, D. Hu, R. Mescall, G. You, D. N. Basov, Q. Dai, M. Liu, *ADV MATER* **2019**, *0*, 1804774.
[45] J. Duan, Y. Li, Y. Zhou, Y. Cheng, J. Chen, *Adv Phys: X* **2019**, *4*, 1593051.
[46] J. M. Atkin, S. Berweger, A. C. Jones, M. B. Raschke, *ADV PHYS* **2012**, *61*, 745.
[47] M. Liu, A. J. Sternbach, D. N. Basov, *REP PROG PHYS* **2017**, *80*, 14501.
[48] E. Wolf, M. Nieto-Vesperinas, *J Opt Soc Am A* **1985**, *2*, 886.
[49] E. H. Synge, *PHILOS MAG* **1931**, *11*, 65.
[50] J. Wessel, *J Opt Soc Am B* **1985**, *2*, 1538.
[51] M. van Exter, A. Lagendijk, *PHYS REV LETT* **1988**, *60*, 49.
[52] S. I. Lysenko, B. A. Snopok, V. A. Sterligov, *Opt Spectrosc* **2010**, *108*, 581.
[53] D. E. Gómez, K. C. Vernon, P. Mulvaney, T. J. Davis, *NANO LETT* **2010**, *10*, 274.
[54] V. A. Sterligov, I. A. Grytsaienko, Y. Men, *OPT LETT* **2016**, *41*, 3710.
[55] N. Kumar, A. Rúa, J. Aldama, K. Echeverría, F. E. Fernández, S. Lysenko, *OPT EXPRESS* **2018**, *26*, 13773.
[56] S. Palomba, L. Novotny, *PHYS REV LETT* **2008**, *101*, 56802.
[57] Y. R. Shen, F. De Martini, *PHYS REV LETT* **1976**, *36*, 216.
[58] R. H. Ritchie, E. T. Arakawa, J. J. Cowan, R. N. Hamm, *PHYS REV LETT* **1968**, *21*, 1530.
[59] C. Ropers, C. C. Neacsu, T. Elsaesser, M. Albrecht, M. B. Raschke, C. Lienau, *NANO LETT* **2007**, *7*, 2784.
[60] S. Sun, Q. He, S. Xiao, Q. Xu, X. Li, L. Zhou, *NAT MATER* **2012**, *11*, 426.
[61] B. Y. Jiang, L. M. Zhang, A. H. Castro Neto, D. N. Basov, M. M. Fogler, *J APPL PHYS* **2016**, *119*, 54305.
[62] Z. Fei, G. O. Andreev, W. Bao, L. M. Zhang, A. S. McLeod, C. Wang, M. K. Stewart, Z. Zhao, G. Dominguez, M. Thiemens, M. M. Fogler, M. J. Tauber, A. H. Castro-Neto, C. N. Lau, F. Keilmann, D. N. Basov, *NANO LETT* **2011**, *11*, 4701.
[63] Z. Fei, A. S. Rodin, G. O. Andreev, W. Bao, A. S. McLeod, M. Wagner, L. M. Zhang, Z. Zhao, M. Thiemens, G. Dominguez, M. M. Fogler, A. H. C. Neto, C. N. Lau, F. Keilmann, D. N. Basov, *NATURE* **2012**, *487*, 82.
[64] G. X. Ni, L. Wang, M. D. Goldflam, M. Wagner, Z. Fei, A. S. McLeod, M. K. Liu, F. Keilmann, B. Özyilmaz, A. H. C. Neto, J. Hone, M. M. Fogler, D. N. Basov, *NAT PHOTONICS* **2016**, *10*, 244.
[65] M. A. Huber, F. Mooshammer, M. Plankl, L. Viti, F. Sandner, L. Z. Kastner, T. Frank, J. Fabian, M. S. Vitiello, T. L. Cocker, R. Huber, *NAT NANOTECHNOL* **2016**, *12*, 207.
[66] P. Hermann, A. Hoehl, G. Ulrich, C. Fleischmann, A. Hermelink, B. Kästner, P. Patoka, A. Hornemann, B. Beckhoff, E. Rühl, G. Ulm, *OPT EXPRESS* **2014**, *22*, 17948.
[67] M. Wagner, D. S. Jakob, S. Horne, H. Mittel, S. Osechinskiy, C. Phillips, G. C. Walker, C. Su, X. G. Xu, *ACS PHOTONICS* **2018**, *5*, 1467.
[68] S. Amarie, T. Ganz, F. Keilmann, *OPT EXPRESS* **2009**, *17*, 21794.
[69] F. Huth, A. Govyadinov, S. Amarie, W. Nuansing, F. Keilmann, R. Hillenbrand, *NANO LETT* **2012**, *12*, 3973.
[70] M. Liu, M. Wagner, J. Zhang, A. McLeod, S. Kittiwatanakul, Z. Fei, E. Abreu, M. Goldflam, A. J. Sternbach, S. Dai, K. G. West, J. Lu, S. A. Wolf, R. D. Averitt, D. N. Basov, *APPL PHYS LETT* **2014**, *104*, 121905.
[71] S. N. Gilbert Corder, X. Chen, S. Zhang, F. Hu, J. Zhang, Y. Luan, J. A. Logan, T. Ciavatti, H. A. Bechtel, M. C. Martin, M. Aronson, H. S. Suzuki, S. Kimura, T. Iizuka, Z. Fei, K. Imura, N. K. Sato, T. H. Tao, M. Liu, *NAT COMMUN* **2017**, *8*, 2262.
[72] S. N. Gilbert Corder, J. Jiang, X. Chen, S. Kittiwatanakul, I. Tung, Y. Zhu, J. Zhang, H. A. Bechtel, M. C. Martin, G. L. Carr, J. Lu, S. A. Wolf, H. Wen, T. H. Tao, M. Liu, *PHYS REV B* **2017**, *96*, 161110.
[73] J. Zhang, A. S. McLeod, Q. Han, X. Chen, H. A. Bechtel, Z. Yao, S. N. Gilbert Corder, T. Ciavatti, T. H. Tao, M. Aronson, G. L. Carr, M. C. Martin, C. Sow, S. Yonezawa, F. Nakamura, I. Terasaki, D. N. Basov, A. J. Millis, Y. Maeno, M. Liu, *PHYS REV X* **2019**, *9*, 11032.
[74] Z. Shi, H. A. Bechtel, S. Berweger, Y. Sun, B. Zeng, C. Jin, H. Chang, M. C. Martin, M. B. Raschke, F. Wang, *ACS PHOTONICS* **2015**, *2*, 790.
[75] O. Khatib, H. A. Bechtel, M. C. Martin, M. B. Raschke, G. L. Carr, *ACS PHOTONICS* **2018**, *5*, 2773.
[76] C. Wu, W. J. Wolf, Y. Levartovsky, H. A. Bechtel, M. C. Martin, F. D. Toste, E. Gross, *NATURE* **2017**, *541*, 511.
[77] S. Amarie, P. Zaslansky, Y. Kajihara, E. Griesshaber, W. W. Schmahl, F. Keilmann, *BEILSTEIN J NANOTECH* **2012**, *3*, 312.
[78] L. Quadrana, J. Almeida, R. Asís, T. Duffy, P. G. Dominguez, L. Bermúdez, G. Conti, J. V. Corrêa Da Silva, I. E. Peralta, V. Colot, S. Asurmendi, A. R. Fernie, M. Rossi, F. Carrari, *NAT COMMUN* **2014**, *5*, 4027.
[79] H. A. Bechtel, E. A. Muller, R. L. Olmon, M. C. Martin, M. B. Raschke, *P NATL ACAD SCI USA* **2014**, *111*, 7191.
[80] P. Hermann, A. Hoehl, G. Ulrich, C. Fleischmann, A. Hermelink, B. Kästner, P. Patoka, A. Hornemann, B. Beckhoff, E. Rühl, G. Ulm, *OPT EXPRESS* **2014**, *22*, 17948.
[81] M. Wagner, Z. Fei, A. S. McLeod, A. S. Rodin, W. Bao, E. G. Iwinski, Z. Zhao, M. Goldflam, M. Liu,

G. Dominguez, M. Thiemens, M. M. Fogler, A. H. Castro Neto, C. N. Lau, S. Amarie, F. Keilmann, D. N. Basov, *NANO LETT* **2014**, *14*, 894.
[82] M. Wagner, A. S. McLeod, S. J. Maddox, Z. Fei, M. Liu, R. D. Averitt, M. M. Fogler, S. R. Bank, F. Keilmann, D. N. Basov, *NANO LETT* **2014**, *14*, 4529.
[83] S. A. Dönges, O. Khatib, B. T. O Callahan, J. M. Atkin, J. H. Park, D. Cobden, M. B. Raschke, *NANO LETT* **2016**, *16*, 3029.
[84] M. A. Huber, M. Plankl, M. Eisele, R. E. Marvel, F. Sandner, T. Korn, C. Schüller, R. F. Haglund, R. Huber, T. L. Cocker, *NANO LETT* **2016**, *16*, 1421.
[85] M. Eisele, T. L. Cocker, M. A. Huber, M. Plankl, L. Viti, D. Ercolani, L. Sorba, M. S. Vitiello, R. Huber, *NAT PHOTONICS* **2014**, *8*, 841.
[86] Z. Yao, V. Semenenko, J. Zhang, S. Mills, X. Zhao, X. Chen, H. Hu, R. Mescall, T. Ciavatti, S. March, S. R. Bank, T. H. Tao, X. Zhang, V. Perebeinos, Q. Dai, X. Du, M. Liu, *OPT EXPRESS* **2019**, *27*, 13611.
[87] A. J. Sternbach, J. Hinton, T. Slusar, A. S. McLeod, M. K. Liu, A. Frenzel, M. Wagner, R. Iraheta, F. Keilmann, A. Leitenstorfer, M. Fogler, H. T. Kim, R. D. Averitt, D. N. Basov, *OPT EXPRESS* **2017**, *25*, 28589.
[88] Y. Liu, R. F. Willis, K. V. Emtsev, T. Seyller, *PHYS REV B* **2008**, *78*, 201403.
[89] V. W. Brar, S. Wickenburg, M. Panlasigui, C. Park, T. O. Wehling, Y. Zhang, R. Decker, Ç. Girit, A. V. Balatsky, S. G. Louie, A. Zettl, M. F. Crommie, *PHYS REV LETT* **2010**, *104*, 36805.
[90] L. Ju, B. Geng, J. Horng, C. Girit, M. Martin, Z. Hao, H. A. Bechtel, X. Liang, A. Zettl, Y. R. Shen, F. Wang, *NAT NANOTECHNOL* **2011**, *6*, 630.
[91] J. Chen, M. Badioli, P. Alonso-Gonzalez, S. Thongrattanasiri, F. Huth, J. Osmond, M. Spasenovic, A. Centeno, A. Pesquera, P. Godignon, A. Z. Elorza, N. Camara, D. A. F. Garcia, R. Hillenbrand, F. H. Koppens, *NATURE* **2012**, *487*, 77.
[92] Z. Fei, A. S. Rodin, W. Gannett, S. Dai, W. Regan, M. Wagner, M. K. Liu, A. S. McLeod, G. Dominguez, M. Thiemens, A. H. Castro Neto, F. Keilmann, A. Zettl, R. Hillenbrand, M. M. Fogler, D. N. Basov, *NAT NANOTECHNOL* **2013**, *8*, 821.
[93] A. Woessner, M. B. Lundeberg, Y. Gao, A. Principi, P. Alonso-Gonzalez, M. Carrega, K. Watanabe, T. Taniguchi, G. Vignale, M. Polini, J. Hone, R. Hillenbrand, F. H. Koppens, *NAT MATER* **2015**, *14*, 421.
[94] G. X. Ni, A. S. McLeod, Z. Sun, L. Wang, L. Xiong, K. W. Post, S. S. Sunku, B. Y. Jiang, J. Hone, C. R. Dean, M. M. Fogler, D. N. Basov, *NATURE* **2018**, *557*, 530.
[95] X. G. Xu, B. G. Ghamsari, J. Jiang, L. Gilburd, G. O. Andreev, C. Zhi, Y. Bando, D. Golberg, P. Berini, G. C. Walker, *NAT COMMUN* **2014**, *5*.
[96] L. Gilburd, X. G. Xu, Y. Bando, D. Golberg, G. C. Walker, *J Phys Chem Lett* **2016**, *7*, 289.
[97] Z. Fei, M. E. Scott, D. J. Gosztola, J. J. Foley, J. Yan, D. G. Mandrus, H. Wen, P. Zhou, D. W. Zhang, Y. Sun, J. R. Guest, S. K. Gray, W. Bao, G. P. Wiederrecht, X. Xu, *PHYS REV B* **2016**, *94*, 81402.
[98] F. Hu, Y. Luan, M. E. Scott, J. Yan, D. G. Mandrus, X. Xu, Z. Fei, *NAT PHOTONICS* **2017**, *11*, 356.
[99] S. Dai, Q. Ma, M. K. Liu, T. Andersen, Z. Fei, M. D. Goldflam, M. Wagner, K. Watanabe, T. Taniguchi, M. Thiemens, F. Keilmann, G. C. A. M. Janssen, S. Zhu, P. Jarillo-Herrero, M. M. Fogler, D. N. Basov, *NAT NANOTECHNOL* **2015**, *10*, 682.
[100] J. D. Caldwell, I. Vurgaftman, J. G. Tischler, O. J. Glembocki, J. C. Owrutsky, T. L. Reinecke, *NAT NANOTECHNOL* **2016**, *11*, 9.
[101] P. Di Pietro, M. Ortolani, O. Limaj, A. Di Gaspare, V. Giliberti, F. Giorgianni, M. Brahlek, N. Bansal, N. Koirala, S. Oh, P. Calvani, S. Lupi, *NAT NANOTECHNOL* **2013**, *8*, 556.
[102] S. Tobias, *J Phys: Condens Matter* **2014**, *26*, 123201.
[103] T. Karzig, C. Bardyn, N. H. Lindner, G. Refael, *PHYS REV X* **2015**, *5*, 31001.
[104] D. Jin, T. Christensen, M. Soljačić, N. X. Fang, L. Lu, X. Zhang, *PHYS REV LETT* **2017**, *118*, 245301.
[105] H. Wang, L. Wang, X. G. Xu, *NAT COMMUN* **2016**, *7*, 13212.
[106] J. Zhang, X. Chen, S. Mills, T. Ciavatti, Z. Yao, R. Mescall, H. Hu, V. Semenenko, Z. Fei, H. Li, V. Perebeinos, H. Tao, Q. Dai, X. Du, M. Liu, *ACS PHOTONICS* **2018**, *5*, 2645.
[107] J. Horng, C. Chen, B. Geng, C. Girit, Y. Zhang, Z. Hao, H. A. Bechtel, M. Martin, A. Zettl, M. F. Crommie, Y. R. Shen, F. Wang, *PHYS REV B* **2011**, *83*, 165113.
[108] L. A. Falkovsky, A. A. Varlamov, *Eur Phys J B* **2007**, *56*, 281.
[109] V. P. Gusynin, S. G. Sharapov, J. P. Carbotte, *NEW J PHYS* **2009**, *11*, 95013.
[110] K. L. Vodopyanov, H. Graener, C. C. Phillips, T. J. Tate, *PHYS REV B* **1992**, *46*, 13194.
[111] T. Elsaesser, J. Shah, L. Rota, P. Lugli, *PHYS REV LETT* **1991**, *66*, 1757.
[112] A. Othonos, *J APPL PHYS* **1998**, *83*, 1789.
[113] M. Mrejen, L. Yadgarov, A. Levanon, H. Suchowski, *SCI ADV* **2019**, *5*, t9618.
[114] K. Kempf, G. Schmieder, G. Kurtze, C. Klingshirn, *Phys Status Solidi B* **1981**, *107*, 297.
[115] J. J. Hopfield, *Phys Rev* **1969**, *182*, 945.
[116] E. Yoxall, M. Schnell, A. Y. Nikitin, O. Txoperena, A. Woessner, M. B. Lundeberg, F. Casanova, L. E. Hueso, F. H. L. Koppens, R. Hillenbrand, *NAT PHOTONICS* **2015**, *9*, 674.
[117] V. J. Sorger, R. F. Oulton, R. Ma, X. Zhang, *MRS BULL* **2012**, *37*, 728.

[118] L. Xiong, C. Forsythe, A. S. McLeod, M. Jung, S. Sunku, G. Ni, S. Liu, M. Fogler, J. H. Edgar, G. Shvets, C. Dean, D. Basov, in *APS March Meeting 2019*, Vol. 64, **2019**.
[119] J. S. Gomez-Diaz, A. Alù, *ACS PHOTONICS* **2016**, *3*, 2211.
[120] S. S. Sunku, G. X. Ni, B. Y. Jiang, H. Yoo, A. Sternbach, A. S. McLeod, T. Stauber, L. Xiong, T. Taniguchi, K. Watanabe, P. Kim, M. M. Fogler, D. N. Basov, *SCIENCE* **2018**, *362*, 1153.
[121] A. V. Nalitov, G. Malpuech, H. Terças, D. D. Solnyshkov, *PHYS REV LETT* **2015**, *114*, 26803.
[122] S. Zhang, H. Wei, K. Bao, U. Håkanson, N. J. Halas, P. Nordlander, H. Xu, *PHYS REV LETT* **2011**, *107*, 96801.
[123] T. Karzig, C. Bardyn, N. H. Lindner, G. Refael, *PHYS REV X* **2015**, *5*, 31001.
[124] M. Saba, C. Ciuti, J. Bloch, V. Thierry-Mieg, R. André, L. S. Dang, S. Kundermann, A. Mura, G. Bongiovanni, J. L. Staehli, B. Deveaud, *NATURE* **2001**, *414*, 731.
[125] G. Messin, J. P. Karr, A. Baas, G. Khitrova, R. Houdré, R. P. Stanley, U. Oesterle, E. Giacobino, *PHYS REV LETT* **2001**, *87*, 127403.
[126] I. De Leon, P. Berini, *PHYS REV B* **2008**, *78*, 161401.
[127] P. M. Bolger, W. Dickson, A. V. Krasavin, L. Liebscher, S. G. Hickey, D. V. Skryabin, A. V. Zayats, *OPT LETT* **2010**, *35*, 1197.
[128] P. Li, I. Dolado, F. J. Alfaro-Mozaz, F. Casanova, L. E. Hueso, S. Liu, J. H. Edgar, A. Y. Nikitin, S. Vélez, R. Hillenbrand, *SCIENCE* **2018**, *359*, 892.
[129] M. Y. Yu, *PHYS REV A* **1983**, *28*, 1855.